**Texas A&M University**
**Mechanical Engineering Department**
**Turbomachinery Laboratory**
**Tribology Group**

# A Destructive Failure Incident and Revamping of Thrust Bearing Test Rig

**TRC-B&C-03-2014**

Research Progress Report to TAMU Turbomachinery Research Consortium

By

**Michael Rohmer**
Research Assistant

**Luis San Andrés**
Mast-Childs Tribology Professor
Principal Investigator

May 2014

**A Test Rig for Evaluation of Thrust Bearings and Face Seals**

TRC Project, TEES # 32513/1519F2

# Executive Summary

To advance thrust bearing technology by providing reliable experimental results to validate predictions, a thrust bearing test rig is being revamped. The original test rig was designed and manufactured to test water lubricated hybrid thrust bearings for USAF Upper Stage Technology Program (2006-2009). Water lubricated the radial bearings holding the rotor and a thrust bearing that reacted loads from the tested bearing. When testing the hybrid thrust bearing with the original test rig, the experimental results correlated very well with the predictions.

In 2013, students converted the thrust bearing test rig to operate with gas lubrication. During its maiden operation, the rotor experienced large vibrations, and the operator initiated an emergency stop, which lead to the failure of the test rig and damage to several components. The large amplitude motions caused the rotor to rub against the flexure pivot, tilting pad journal bearings, the slave thrust bearing, and the air buffer seals. The contact caused foreign material to weld onto the surface of the rotor, the tilting pads of the air lubricated journal bearings to weld to the bearing cartridge, the surface of the slave thrust bearing to be damaged, and the air buffer seal screws to shear off the housing. The emergency stop placed a large torsion on the coupling causing its flexible diaphragm to rupture.

An electroplating company grinded the welded foreign material off the rotor, chromeplated thin-dense chrome onto the rotor, and grinded back to its original dimensions. A balancing company then balanced the rotor. The original manufacturer replaced the flexible diaphragm of the coupling and rebalanced it. The original, water lubricated journal bearings replaced the damaged air journal bearings. A campus machine shop lapped the face of the slave thrust bearing to provide a smooth surface. With the repaired and replaced components, the test rig underwent assembly. Once the test rig is completely functioning, it will be used to measure the static and dynamic performance of a water lubricated hybrid thrust bearing. The test rig could also be used to test an oil lubricated thrust bearing or other thrust bearings with a 3-inch outer diameter at speeds up to 20 krpm and loads up to 600 newtons.

# Table of Contents

# List of Tables



# List of Figures

# Introduction

Thrust bearings are vital components in turbomachinery as they support axial loads and control shaft position. In turbomachinery, axial loads are dependent on shaft speed and pressure. The prediction of these axial loads is largely empirical, creating the need for reliable thrust bearings in any turbomachine. To enhance thrust bearing technology, TAMU designed and built a thrust bearing test rig to supply reliable experimental results to validate predictive tools [1].

USAF (2006-2009) funded a project to design and construct a water lubricated thrust bearing test rig for measurement of the forced performance of hybrid thrust bearings operating at high supply pressure and high rotational speed. The test hybrid thrust bearings exhibited remarkable correlation with the predictive tool [2].

In 2013, the thrust bearing test rig, modified to operate with air lubricated bearings, experienced large vibrations leading to severe damage [3]. In order to use the current equipment to continue providing reliable experimental results for various types of thrust bearings, the test rig is presently revamped. This report describes concepts for other thrust bearing test rigs, the current test rig and its components, the failure of the test rig, and the damage and repairs made to components of the test rig. Once the test rig is functioning, it will be used to measure the static and dynamic performance of a water lubricated hybrid thrust bearing. The test rig could also be used to test an oil lubricated thrust bearing or other thrust bearings with a 3-inch outer diameter at speeds up to 20 krpm.

# A Review of Thrust Bearing Test Rigs

There are two types of rigs to test thrust bearings: rigs with one thrust bearing, and rigs with multiple thrust bearings. In the first type, one thrust bearing applies a load to a collar on a spinning shaft. In the second type, two thrust bearings apply opposite loads to collars mounted on a spinning shaft. Typically test rigs with one thrust bearing have a vertical orientation, and test rigs with multiple thrust bearings have a horizontal orientation.

Gregory (1974) [4] describes a rig that uses two double thrust bearings to test oil lubricated hydrostatic thrust bearings, as shown in Figure 1. This rig consists of two separate housings: a sliding housing and a fixed housing. Each housing holds a double face thrust bearing and a journal bearing. A hydraulic system transmits a load to the sliding housing, which causes its thrust bearing to apply the load to the rotor thrust collar. The rotor exerts the same load on the thrust bearing in the fixed housing. The fixed housing holds its double thrust bearing stationary. A flexible coupling,

connecting the shaft to the motor, isolates the motor from loads applied to the rotor. Thermocouples within the pads, in the supply line, and in the drain line measure the pad temperatures and bearing power loss at various loading pressures and shaft speeds. Eddy current sensors in one pad of a loaded thrust bearing measure the oil film thickness.

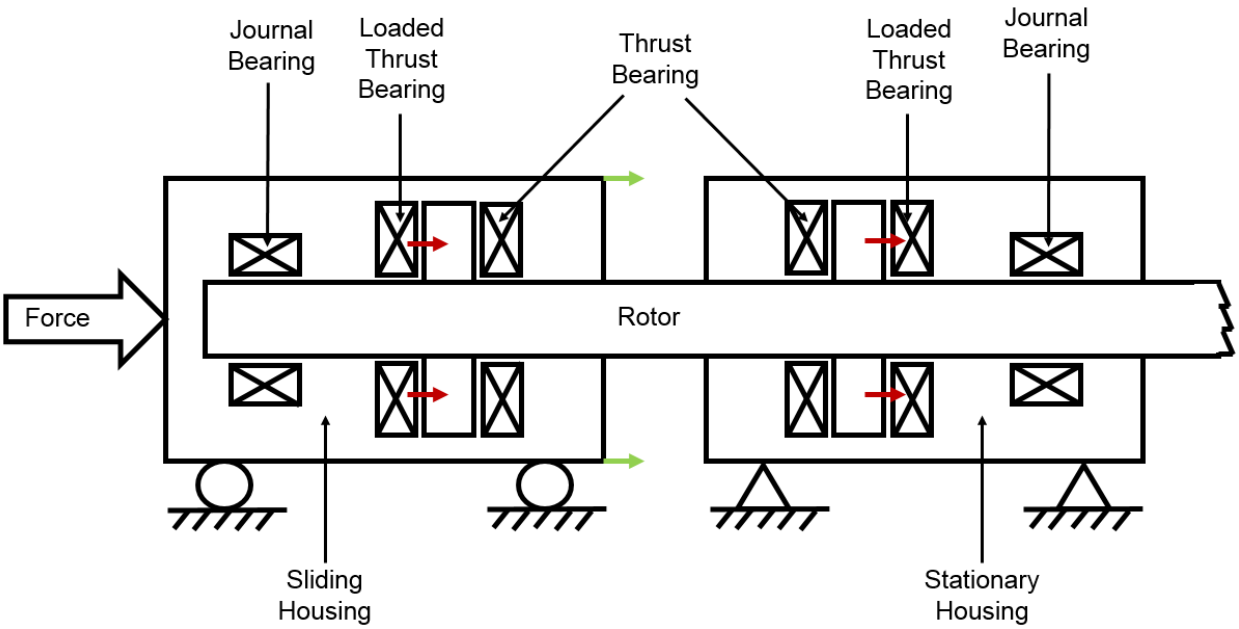


**Figure 1. Schematic view of multiple thrust bearing test rig, after Gregory [4]. The arrows between the thrust bearings and thrust collars denote transferred axial forces, and the arrows on the housing denote its axial movement.**

Glavatskih (2002) [5] introduces a rig that uses two thrust bearings facing away from each other, as depicted in Figure 2. The schematic view does not show the journal bearings that hold the shaft radially as they are outside of the housing. Rolling element bearings support the housing, allowing it to rotate freely. A belt attaches the shaft to the motor. Four hydraulic cylinders force the guiding holders and the thrust bearings in opposite directions. The thrust bearings apply the load to the rotor in opposite directions. A load cell, attached to the housing, measures the torque. One of the thrust bearings houses thermocouples, pressure sensors, and eddy current sensors to measure the bearing pad temperature, pressure profile, and clearance between the thrust bearing and thrust collar.

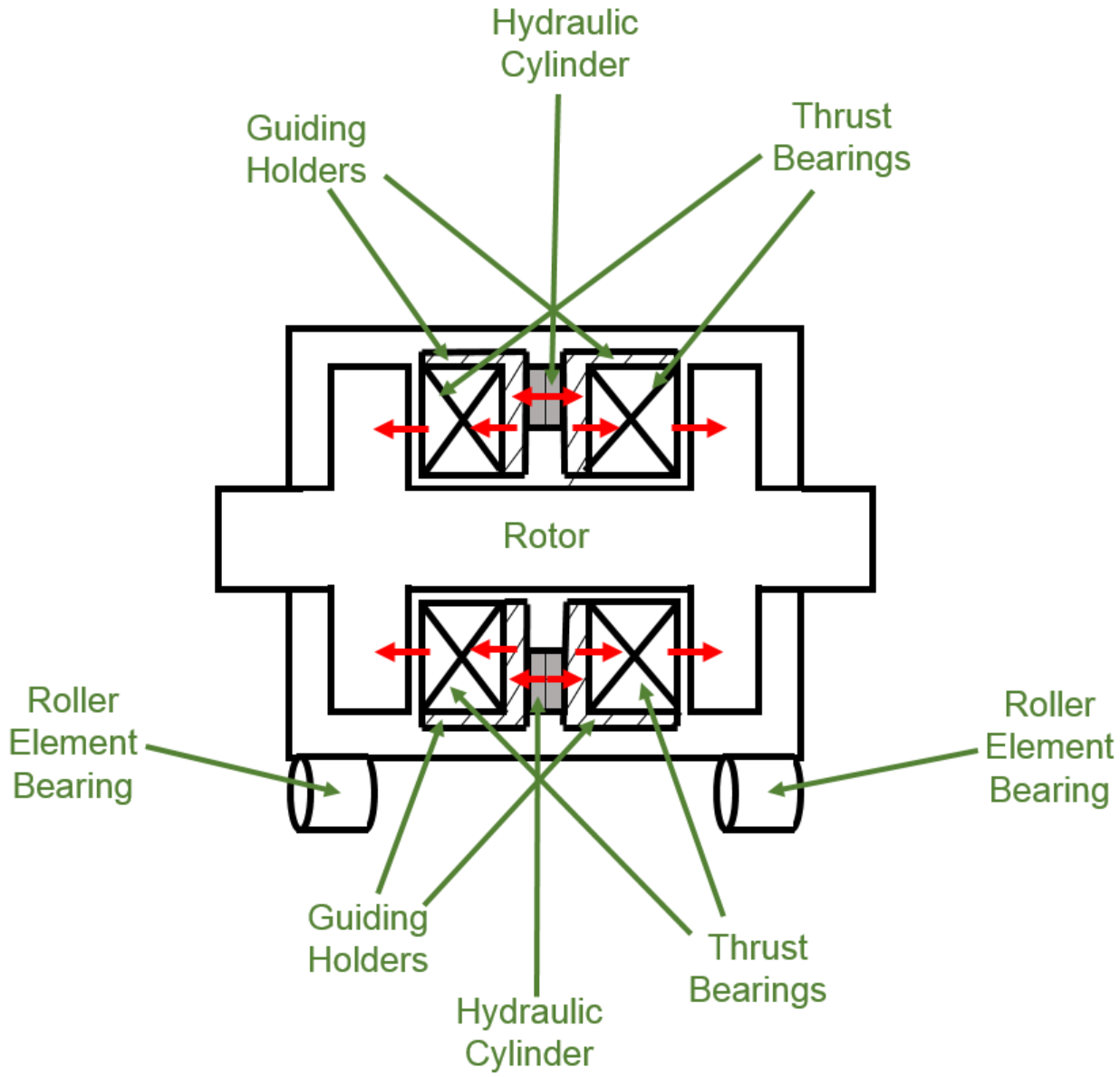


**Figure 2. Schematic view of double-sided thrust bearing test rig, after Glavatskih [5]. Arrows denote transferred axial forces.**

Dykas and Tellier (2008) [6] describe a rig that uses one thrust bearing to apply loads, as shown in Figure 3. A motor spindle spins a shaft with a thrust runner; and a pneumatic loader pushes on the non-rotating shaft and thrust bearing through a ball loading contact. Air bearings radially position the non-rotating shaft. A torque arm and load cell measure the torque applied to the bearing. A furnace encloses the thrust runner on the rotating shaft and the thrust bearing on the non-rotating shaft. Dadouche, Fillon, and Dmochowski (1999) [7] and Balducchi (2013) [8] describe similar type test rigs.

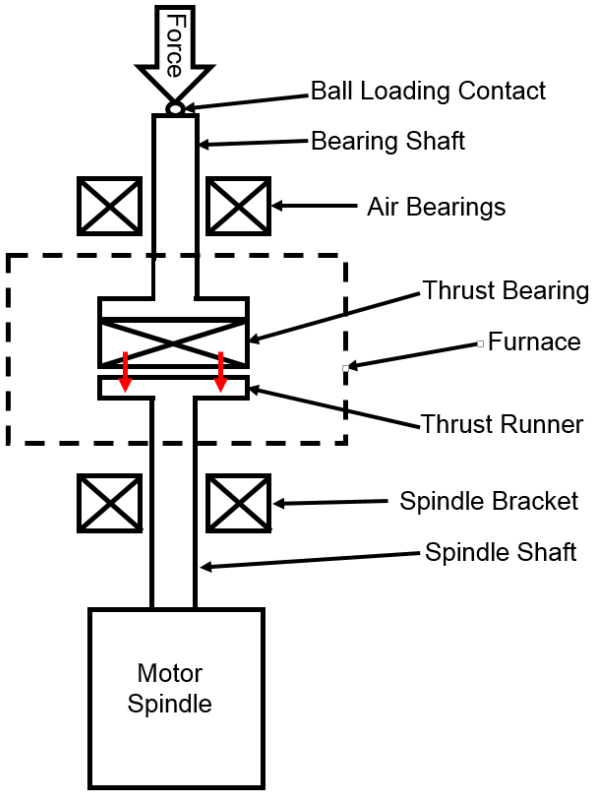


**Figure 3. Schematic view of test rig, after Dykas and Tellier [6]. Arrows depict transferred axial forces.**

## Description of TAMU Thrust Bearing Test Rig [1]

Similar to the test rigs by Gregory [4] and Glavaskith [5], the TAMU thrust bearing test rig has a horizontal configuration with two thrust bearings, as shown in the cross sectional view in Figure 4. As the test rig shown in Ref [4] (Figure 1), the TAMU test rig uses an axially translating thrust bearing, the test thrust bearing, to apply a load and a stationary thrust bearing, the slave thrust bearing, to react the load. Both thrust bearings face the outer side of the thrust collars on the rotor. Table 1 lists the main components of the test rig, and Figure 5 shows how it operates. A motor and quill coupling drive the test rotor comprised of a 197 mm long 304 stainless steel shaft with two press-fitted thrust collars. The shaft diameter at the location of the radial bearings is 38.1 mm, while the thrust collars have an outer diameter equal to 102 mm and 107 mm. Two radial hybrid bearings support the test rotor, whose center of mass locates at mid span between the two bearings. Through a non-rotating floating shaft, a hydraulic shaker delivers an axial load (static and/or dynamic) to the test thrust bearing. Two aerostatic radial bearings support the axial load shaft with

minimal friction. The test thrust bearing moves axially to impose the load on the rotor thrust collar. This axial load is then reacted by the slave thrust bearing rigidly affixed to a bearing support [1].

The electric drive motor is rated at 22 kW at its top speed of 30 krpm. The motor can deliver a constant torque, maximum 700 N-cm, over the entire speed range. A digital closed-loop speed control with LabView® interface and a water chiller for cooling are included. A commercial vendor designed the coupling to have a very low axial stiffness (3.5 N/mm) with an allowance of 0.61 to 1.22 mm axial travel. These characteristics permit isolating the motor from the axial loads imposed on the test thrust element [1].

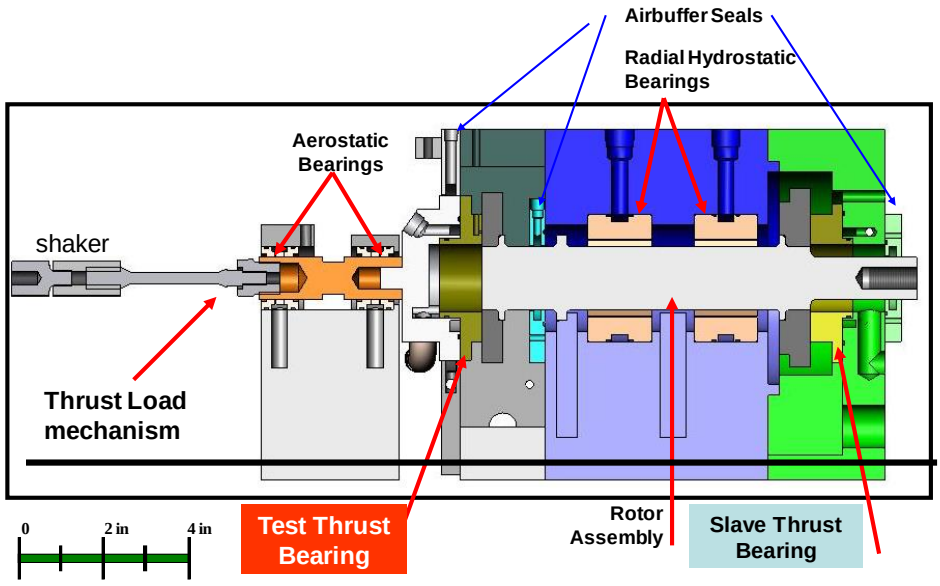


**Figure 4. Cross section view of TAMU thrust bearing test rig [1].**

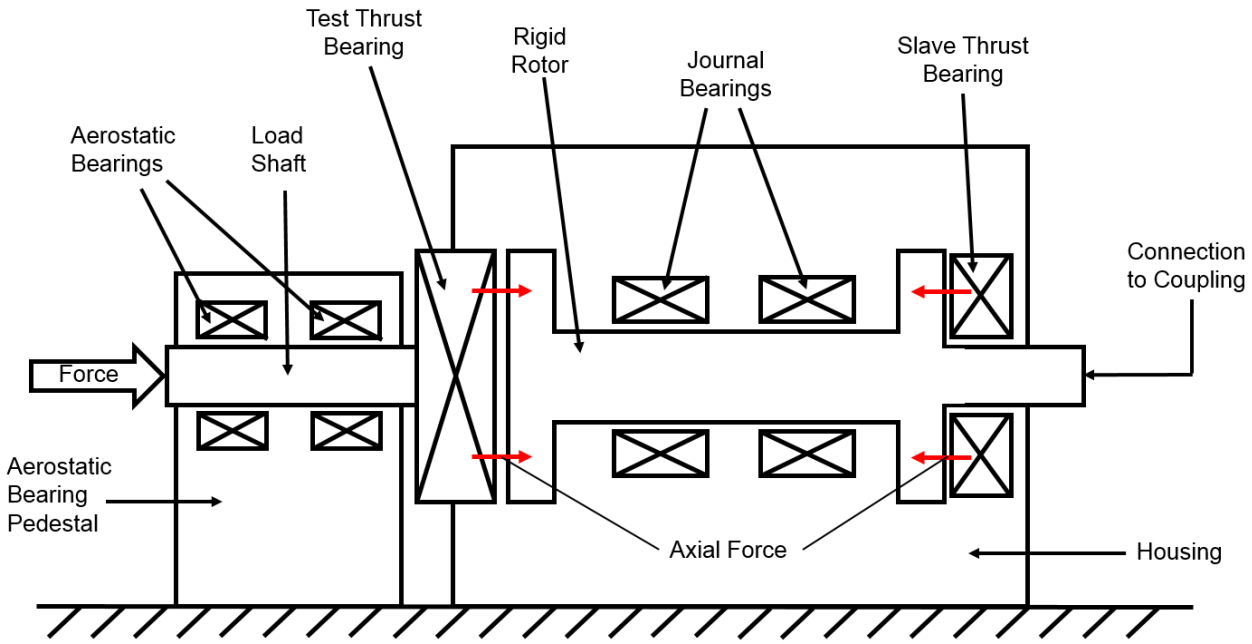


**Figure 5. Schematic view of thrust bearing test rig. Arrows depict path of axial force.**

**Table 1. Main components of the thrust bearing test rig.**

| Part | Quantity | Fig. # |
|---|---|---|
| Rotor | 1 | 6 |
| Flexure Pivot, Hydrostatic Tilting Pad Journal Bearings | 2 | 7 |
| Journal Bearing Housing | 1 | 8 |
| Slave Thrust Bearing | 1 | 9 |
| Slave Bearing Housing | 1 | 10 |
| Air Buffer Seals | 2 | 12 |
| Test Thrust Bearing | 1 | 13 |
| Thrust Bearing Housing | 1 | 14 |
| Thrust Bearing Cover | 1 | 15 |
| Load Shaft | 1 | 17 |
| Aerostatic Bearings | 2 | 17 |
| Aerostatic Bearing Pedestal | 1 | 17 |

Figure 6 shows the rotor assembly that weighs 3.86 kg and is 26.04 cm in length. A flexible coupling threads into the end of the rotor. Two flexure pivot, tilting pad hydrostatic bearings

radially support the rotor. Two hybrid thrust bearings apply loads to the outside of each thrust collar.

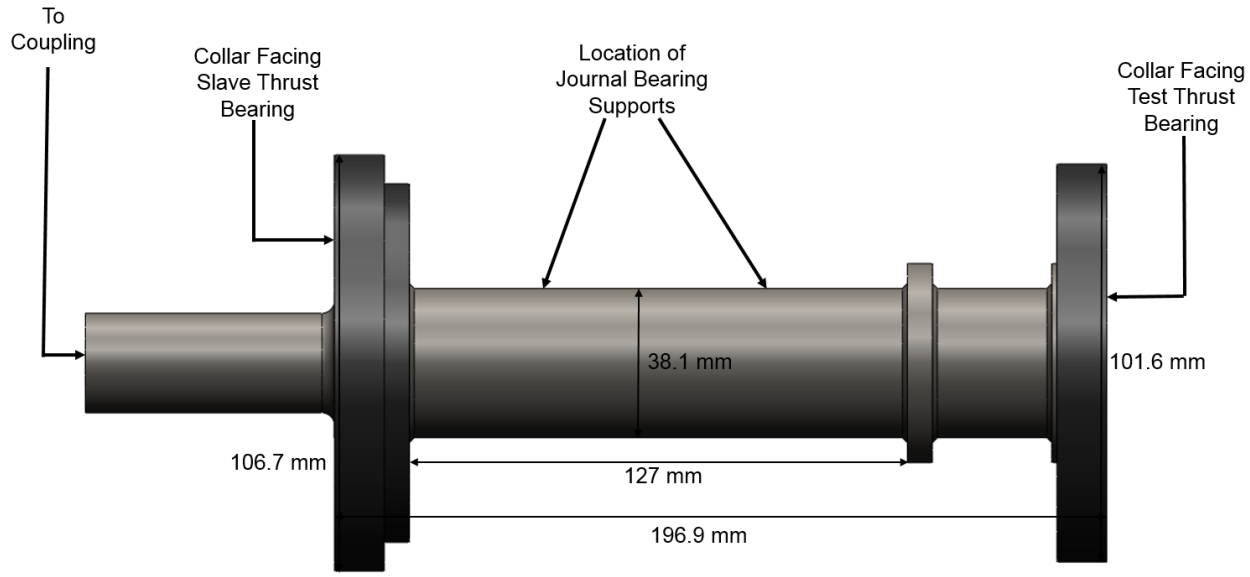


**Figure 6. Rotor with key dimensions and labeled parts [9].**

Figure 7 shows the 330 bearing bronze, flexure pivot, tilting pad hydrostatic journal bearings and Table 2 lists the specifications. Figure 8 shows the journal bearings installed in the 304 stainless steel split journal bearing housing, which directs lubricant to and away from the bearings. Externally pressurized water at ambient temperature lubricates the bearings. Bolts attach the journal bearing housing to the table.

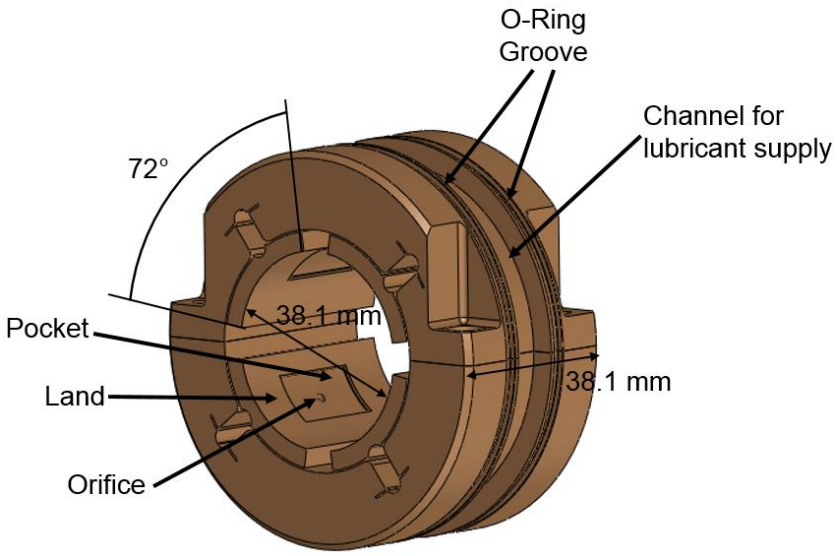


**Figure 7. Water lubricated flexure pivot pad hydrostatic journal bearings with key dimensions and features labeled [9].**

**Table 2. Specifications of flexure pivot, tilting pad hydrostatic bearings [9].**

| | | | |
|---|---|---|---|
| Nominal | Radial Clearance | 3 mil | 76.2 μm |
| Bearing | Inner Diameter | 1.50 inch | 38.1 mm |
| | Outer Diameter | 3.00 inch | 76.2 mm |
| | Length | 1.50 inch | 38.1 mm |
| Pads | Number of Pads | 4 | |
| | Arc Length | 72° | |
| | Pivot Offset (dim) | 60% arc length | |
| | Preload (dim) | 0.20 | |
| | Flexure Stiffness | 1770 lb-in/rad | 200 Nm/rad |
| Pockets (one per pad) | Axial Length | 0.50 inch | 12.7 mm |
| | Arc Length | 24° | |
| | Depth | 20 mil | 508 μm |
| | Mean Diameter | 2.16 inch | 54.9 mm |
| | Pocket/Wetted Area Ratio | 0.11 | |
| Orifices (one per pocket) | Diameter | 0.067 inch | 1.702 mm |
| | Radial Injection | 50% of pocket length | |

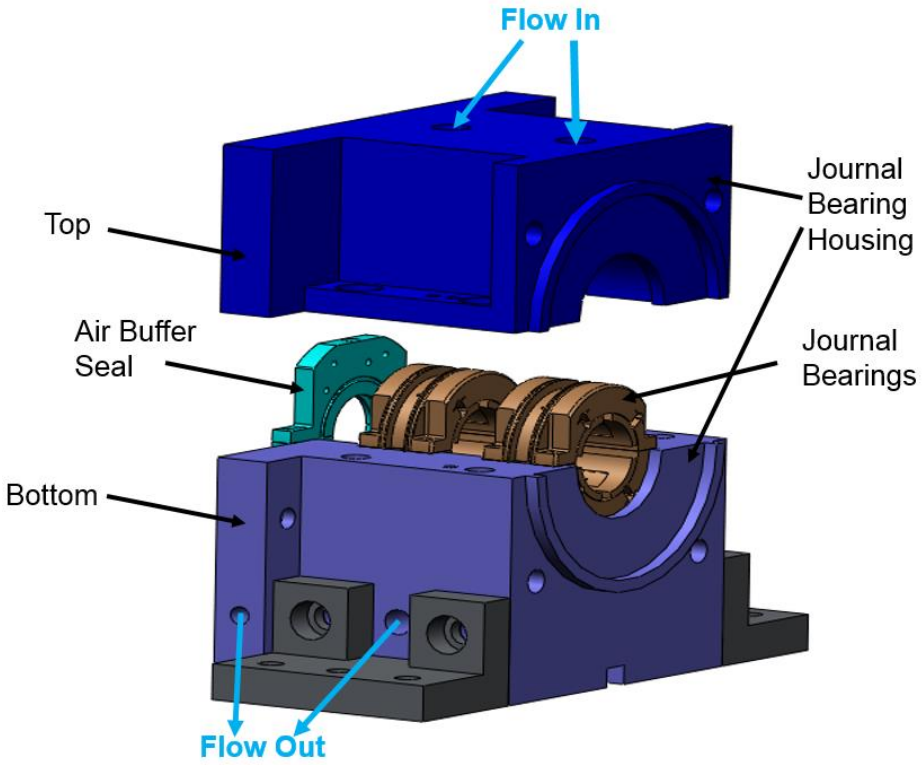


**Figure 8. Exploded view of journal bearing housing with journal bearings and air buffer seal included.**

Figure 9 shows the 660 bronze slave thrust bearing and Table 3 lists its specifications. Figure 10 shows screws connecting the slave bearing to the 304 stainless steel slave bearing housing, which directs lubricant to and away from the slave thrust bearing. The slave thrust bearing has holes to install three eddy current sensors that will measure the operating clearance between the slave bearing and the rotor thrust collar. Bolts attach the slave bearing housing to the journal bearing housing and to the table.

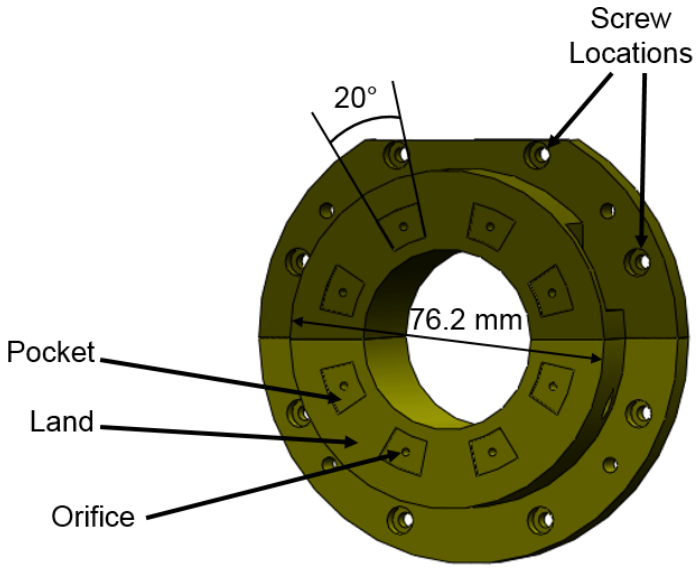


**Figure 9. Slave bearing with key dimensions labeled [9].**

**Table 3. Specifications of test and slave thrust bearing [9].**

| | | | |
|---|---|---|---|
| Nominal | Axial Clearance | 3 mil | 76.2 μm |
| Bearing | Inner Diameter | 1.60 inch | 40.6 mm |
| | Outer Diameter | 3.00 inch | 76.2 mm |
| | Axial Clearance | 0.5–5.5 mil | 13-140 μm |
| Pockets | Number of Pockets | 8 | |
| | Mean Diameter | 2.16 inch | 54.9 mm |
| | Radial Length | 0.32 inch | 8.13 mm |
| | Arc Length | 20° | |
| | Depth | 17.5 mil / 20 mil | 444.5 μm / 508 μm |
| | Pocket/Wetted Area Ratio | 0.19 | |
| Orifices (one per pocket) | Diameter | 0.071 inch | 1.80 mm |
| | Radial Injection | 1.08 inch | 27.4 mm |

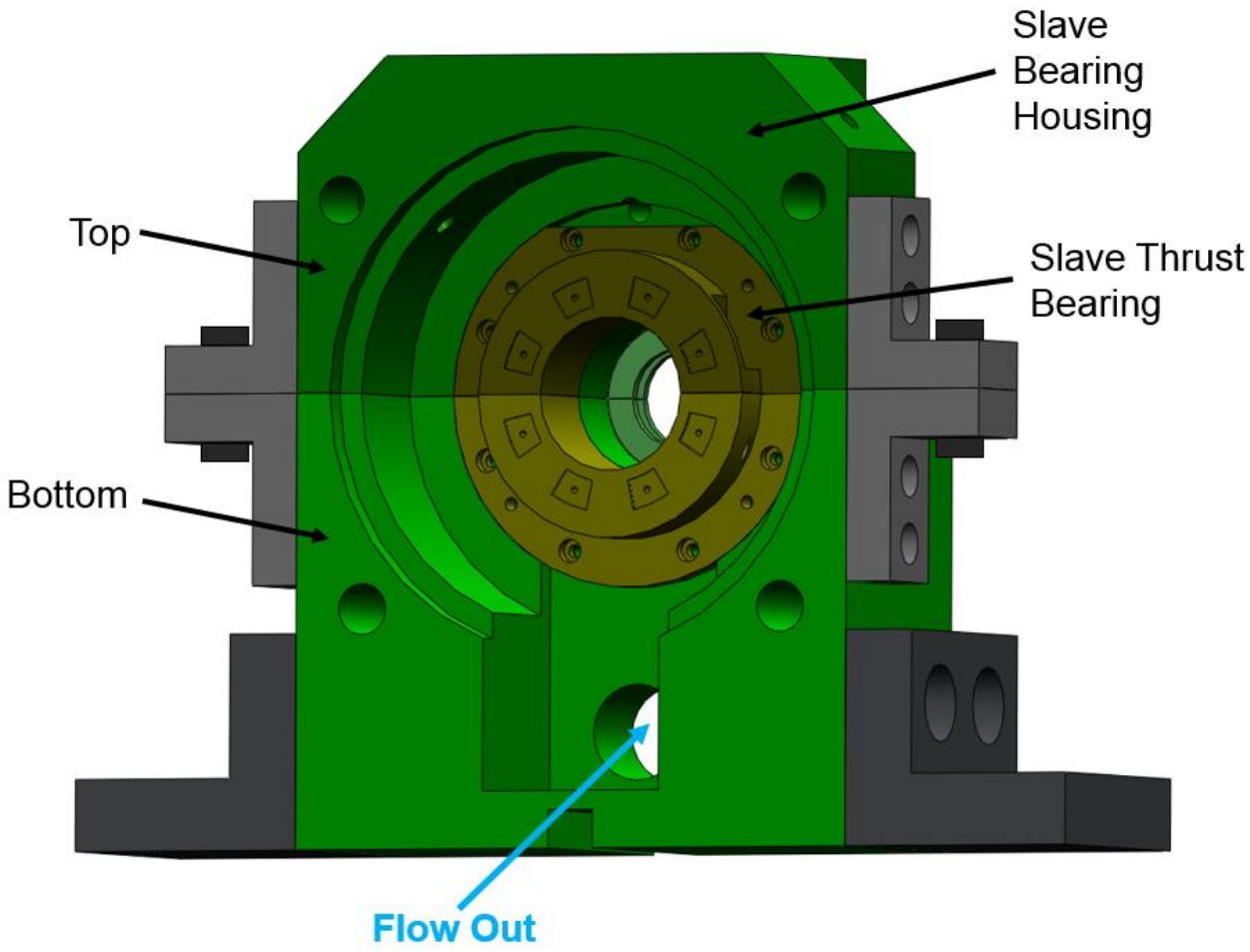


**Figure 10. Bearing housing with the slave thrust bearing installed [9].**

Figure 11 shows two 660 bronze air buffer seals on the slave and journal bearing housings. Pins align each half of the air buffer seals, and screws fasten the two halves together to form the air buffer seals, as shown in Figure 12. Pins also align the air buffer seals to fit onto the housings.

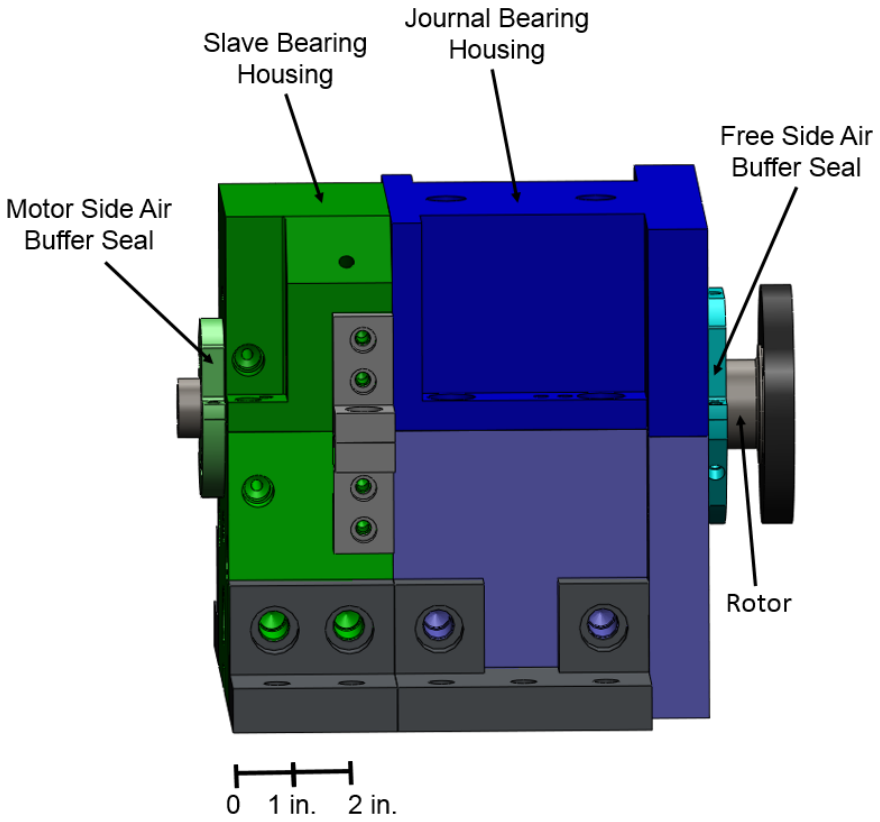


**Figure 11. Assembly of slave thrust bearing housing and journal bearing housing with end seals installed.**

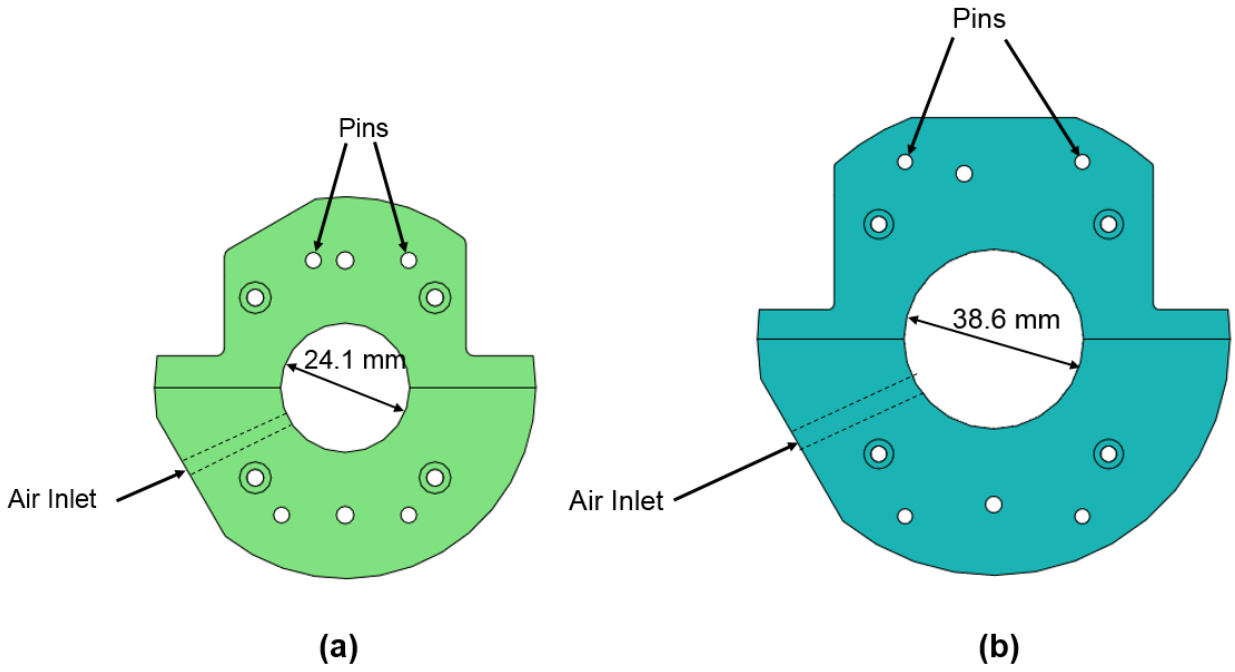


**Figure 12. (a) Air buffer seal on the motor drive end. (b) Air buffer seal on the rotor free end.**

Figure 13 shows the 660 bronze test thrust bearing and Table 3 lists its specifications. Screws connect the test bearing to the load shaft (see Figure 17). The test bearing has holes for three eddy current sensors that will measure the operating clearance between the bearing and the thrust collar. There are holes for four pressure transducers, two in the lubricated lands and two in the pockets, to measure the static pressure. The sensors will measure the static pressure in the bearing.

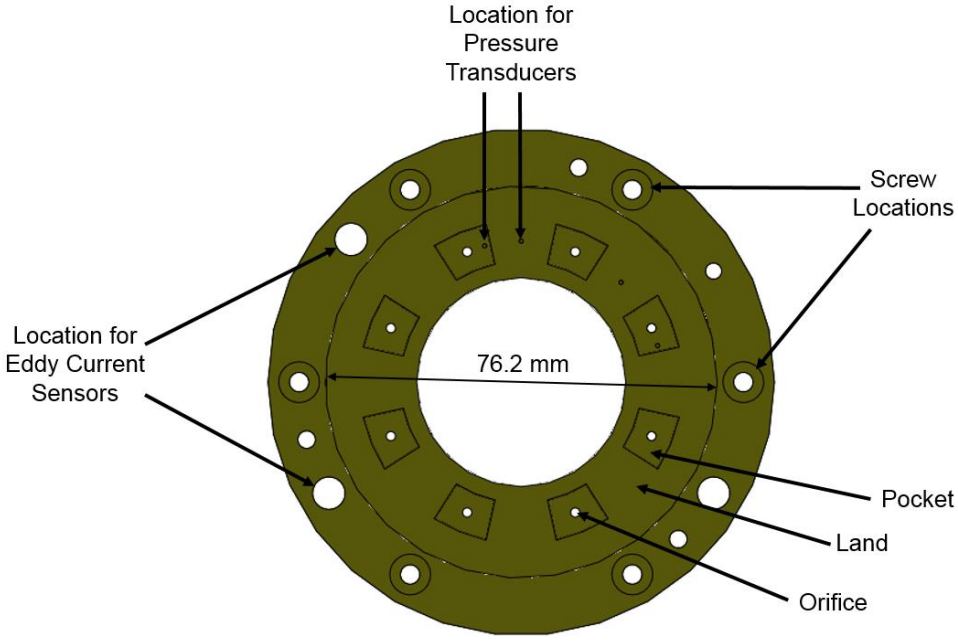


**Figure 13. Test bearing with diameter and key features labeled [9].**

Figure 14 shows the 304 stainless steel test bearing housing directing lubricant away from the test thrust bearing. Figure 15 shows the 304 stainless steel cover and air buffer seal that go around the test bearing (see Figure 14). Bolts connect the test bearing housing to the journal bearing housing and the table, and they connect the cover and air buffer seal to the test bearing housing.

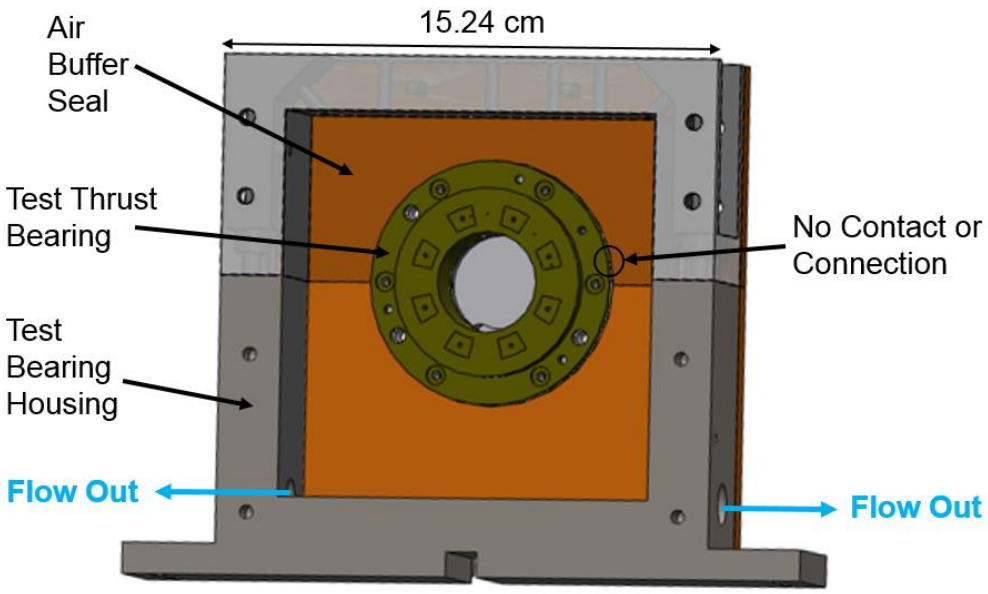


**Figure 14. Test bearing housing with bearing shown.**

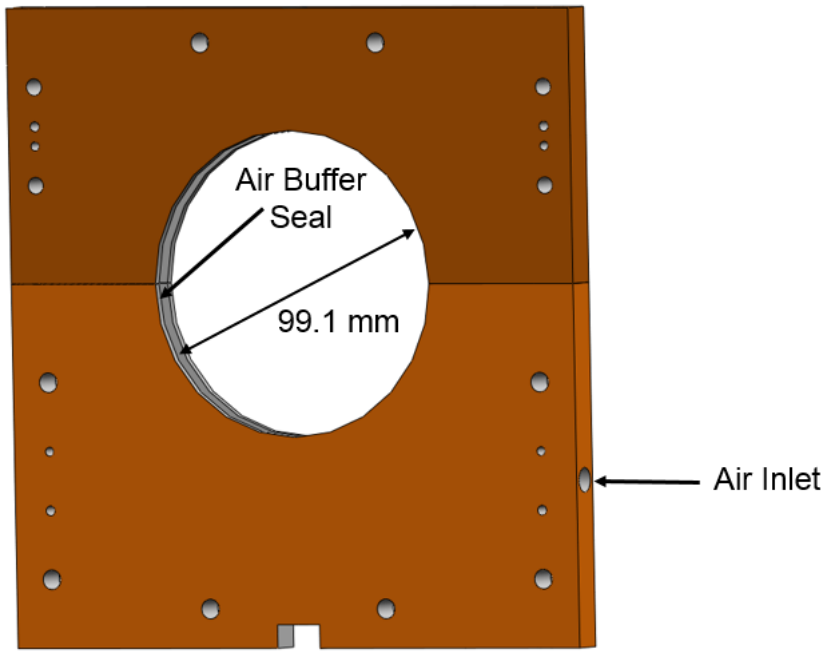


**Figure 15. Cover and air buffer seal around test bearing.**

The complete housing assembly, shown in Figure 16, is made of the journal bearing housing, the slave bearing housing and the test bearing housing. The housing has holes for seven eddy

current sensors, four in the radial direction and three in the axial direction. The test thrust bearing also has holes for three eddy current sensors to measure displacement in the axial direction. Also, pressure transducers and thermocouples measure the temperature and pressure of the flow going into the bearings. Flow meters measure the flow rate entering and exiting the test thrust bearing.

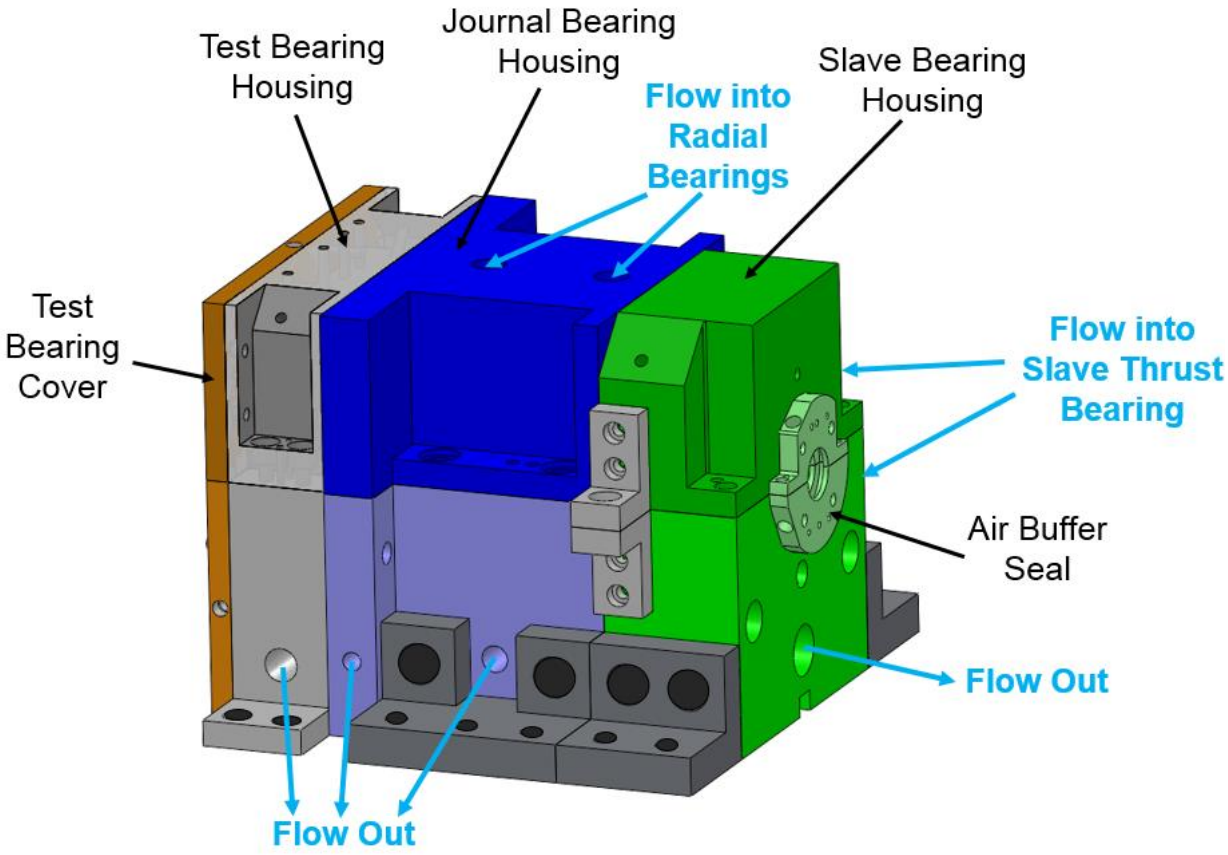


**Figure 16. Assembly of journal bearing housing, slave bearing housing, and test bearing housing.**

Figure 17 shows an assembly of the test thrust bearing, the Inconel 718 load shaft, 660 bronze aerostatic journal bearings, and the 4140 alloy steel aerostatic bearing pedestal. The 718 Inconel load shaft, 25.5 mm in diameter and 85.7 mm long, holds the test thrust bearing. A connection to a hydraulic shaker enables the test bearing to apply an axial load to the rotor. Two aerostatic bearings radially support the load shaft. The aerostatic bearings have an inner diameter of 25.43 mm, a diametrical clearance of 25.4 μm, an outer diameter of 31.75 mm, and a length of 22.2 mm. The aerostatic journal bearings are installed in the bearing pedestal that is connected to the table.

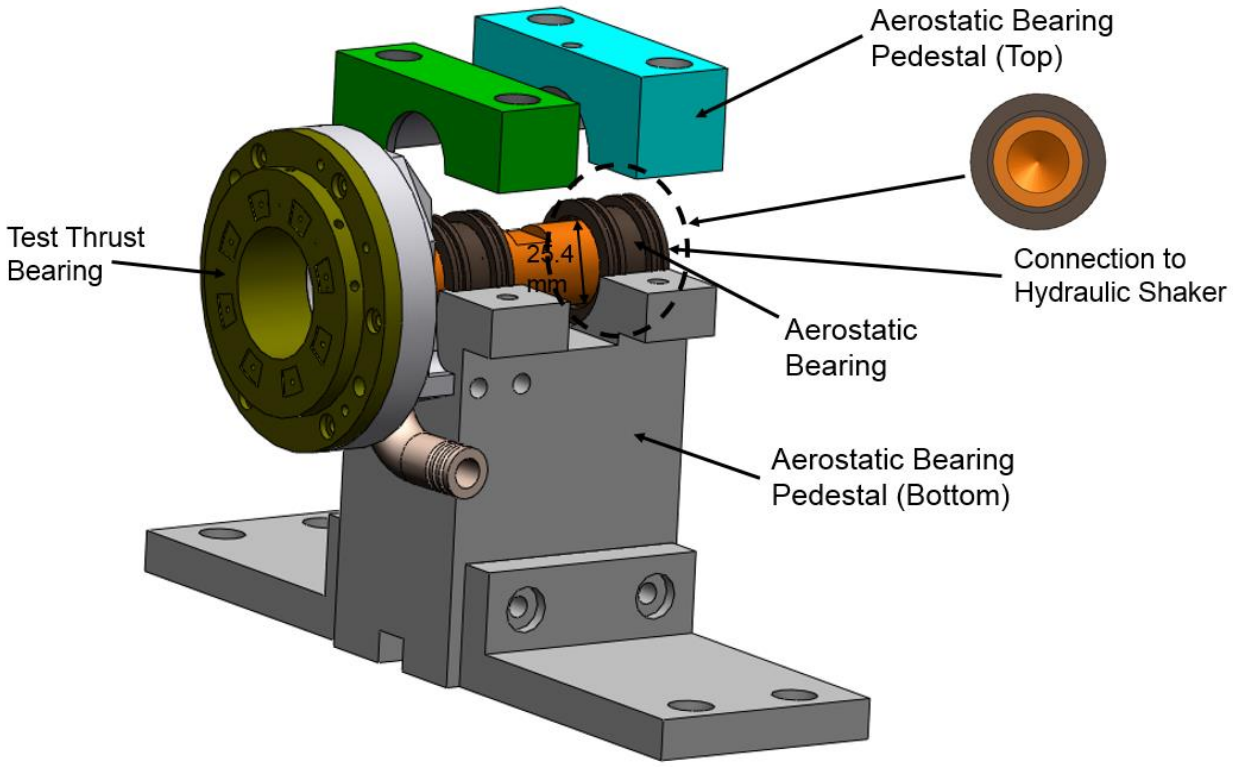


**Figure 17. Assembly of test thrust bearing, load shaft, and aerostatic bearings in bearing pedestal.**

## Test Rig Failure

In 2012-2013, after several months of effort, hydrostatic journal bearings were designed and manufactured to operate with air lubrication, as shown in Figure 18. The bearings are flexure pivot with hydrostatic pressurization and have no pockets. During its maiden operation with the new journal bearings installed, the shaft accelerated to 25,000 RPM with a supply pressure to the air bearings ranging from 4.14 to 6.89 bar. Figure 19 shows the measured amplitude of rotor motion at the motor side versus rotor speed and for various supply pressures into the journal bearings. The figure shows a critical speed at around 6,000 RPM. In addition, the amplitude of the rotor at 4.14 bar begins to increase at 26,000 RPM. Significant sub-synchronous motions starting at 14,000 Hz were recorded during the measurements. While operating at a supply pressure of 4.14 bar, the shaft was stable to 27,000 RPM. The amplitude of the discrete fourier transform (DFT) of the motor side at a speed of 27,000 RPM and a supply pressure of 4.14 bar can be seen in Figure 20. The motion of the system is mostly synchronous with an overall amplitude of one mil (25 μm). At a shaft speed of 28,000 RPM, the test rig made a loud noise from the shaft contacting the bearings,

and then immediately the operator applied the emergency stop. The large amplitude motions caused the flexure pads to weld to the bearing cartridge, the bolts holding the air buffer seals to shear off, and extensive the rotor to experience extensive surface damage. The abrupt emergency stop caused the diaphragm of the flexible coupling to rupture because the high change of angular momentum occurred in such a short time [3].

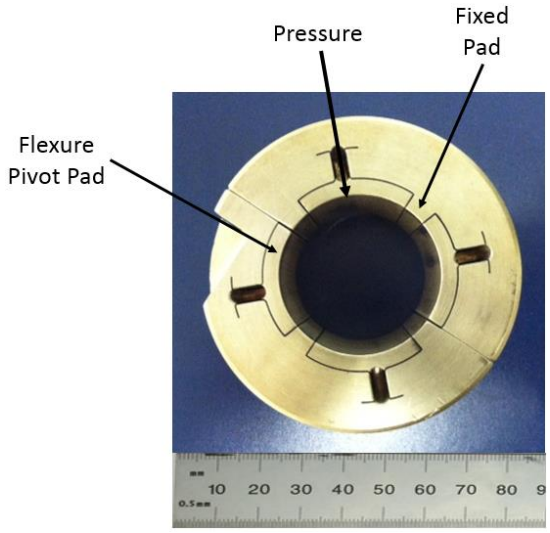


**Figure 18. Air lubricated journal bearings [1].**

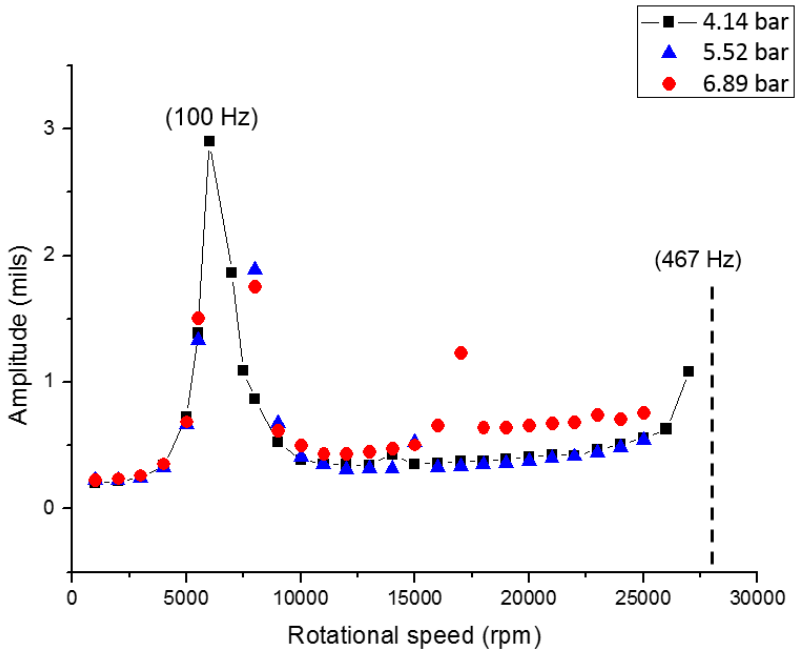


**Figure 19. Amplitude of rotor motion at the motor side vs. rotor speed for operation at various supply pressures. Rotor supported on air bearings [3].**

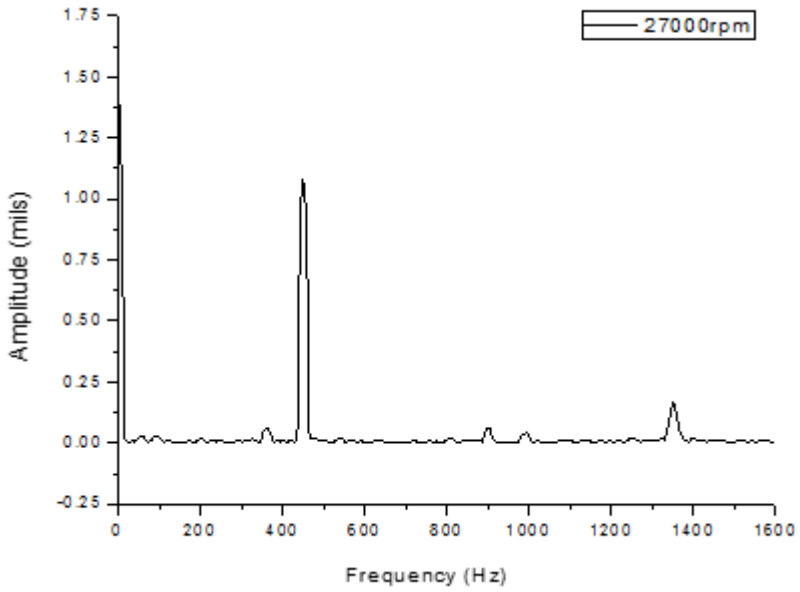


**Figure 20. Amplitude of DFT of the motor side at a rotor speed of 27,000 RPM and supply pressure of 4.14 bar with the rotor supported on air bearings [3].**

Aside from the large synchronous amplitude motions, significant sub-synchronous amplitude motions were recorded during the measurements. Figure 21 shows waterfall plots of the rotor motion at the motor side at supply pressures of 4.14 bar, 5.52 bar, and 6.89 bar. With a supply pressure of 6.89 bar, sub-synchronous motions are dominant at 16,000 RPM and 17,000 RPM and persist at ~125 Hz. With a supply pressure of 5.52 bar, a sub-synchronous motion is dominant at 15,000 RPM and persists at ~125 Hz. With a supply pressure of 4.14 bar, a small sub-synchronous motion at 14,000 RPM persists at ~ 75 Hz.

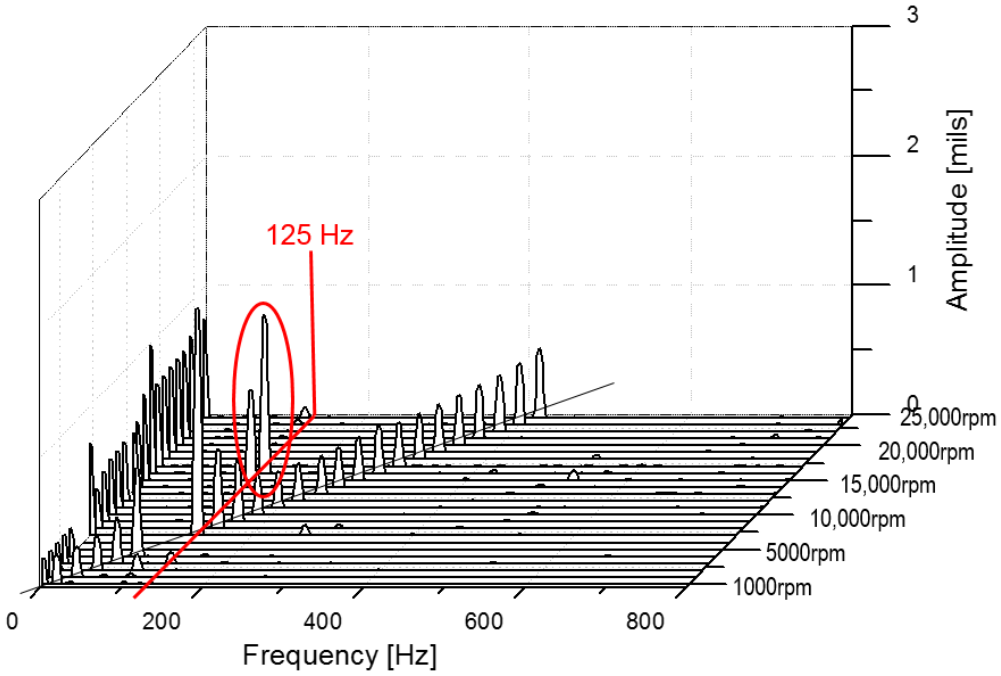
125 Hz
Amplitude [mils]
3
2
1
0
25,000rpm
20,000rpm
15,000rpm
10,000rpm
5000rpm
1000rpm
0
200
400
600
800
Frequency [Hz]

**(a)**

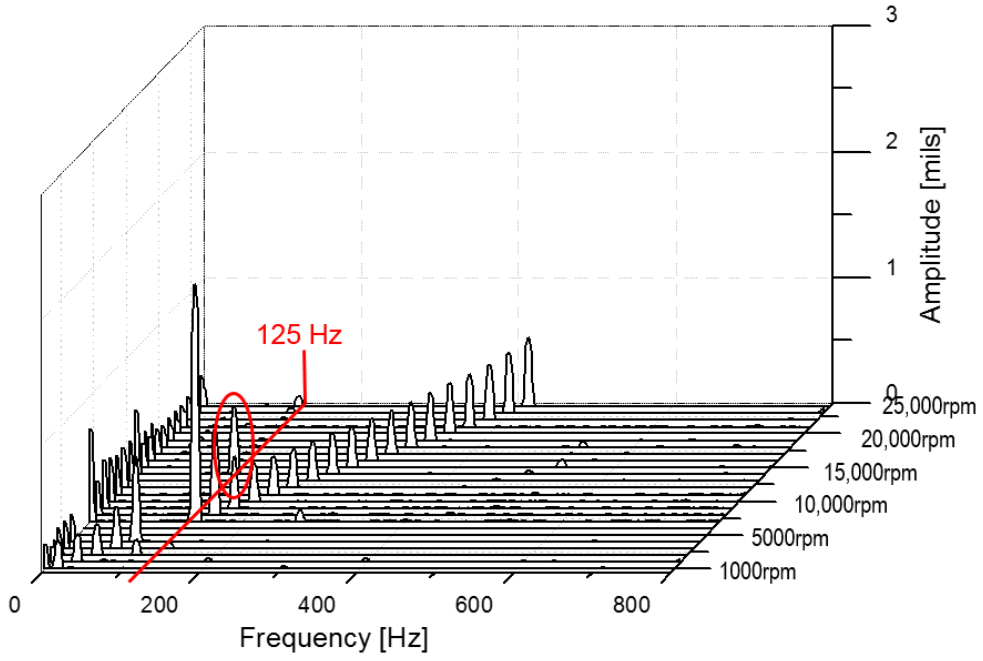
125 Hz
Amplitude [mils]
3
2
1
0
25,000rpm
20,000rpm
15,000rpm
10,000rpm
5000rpm
1000rpm
0
200
400
600
800
Frequency [Hz]

**(b)**

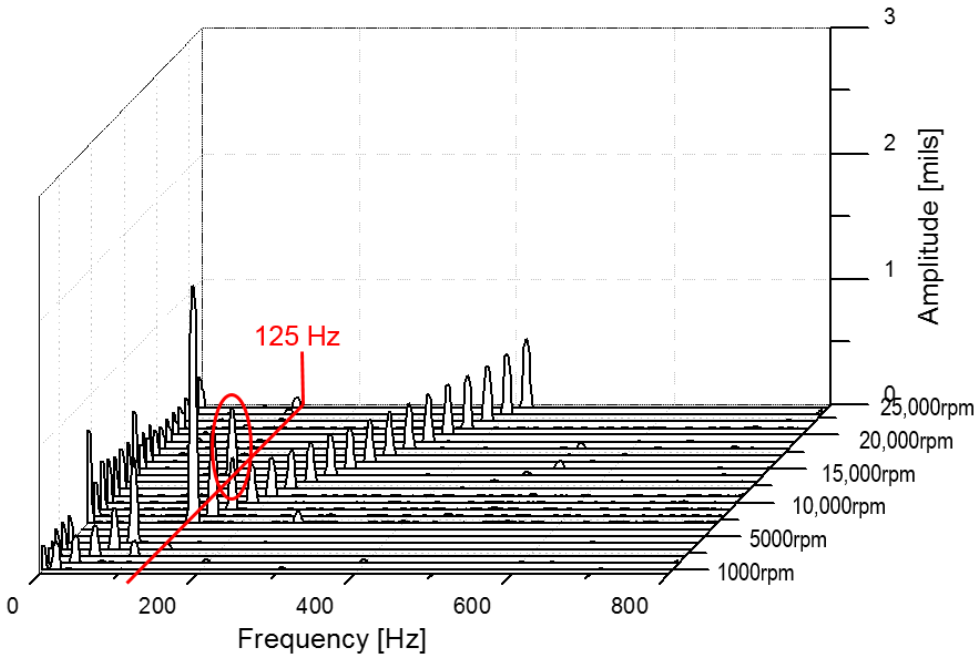


**(c)**

**Figure 21. Waterfall plot of amplitude of DFT of the motor side at increasing rotor speeds and an operation supply pressure of (a) 6.89 bar, (b) 5.52 bar, and (c) 4.14 bar. Rotor supported on air bearings. Circle indicates significant sub-synchronous motions [3].**

# Repairs and modifications

## Rotor

Figure 22 shows the damaged rotor. During the failure, large amplitude motions forced the rotor to contact the air buffer seals, the eddy current sensors, and most notably the journal bearings. At the locations of the air buffer seals and the eddy current sensors, the air buffer seals and eddy current sensors deposited foreign material on the rotor. At the locations of the journal bearings, the shaft damage was more significant. The friction from contact produced significant heat between the rotor and the journal bearings, causing each component material to weld onto other components.

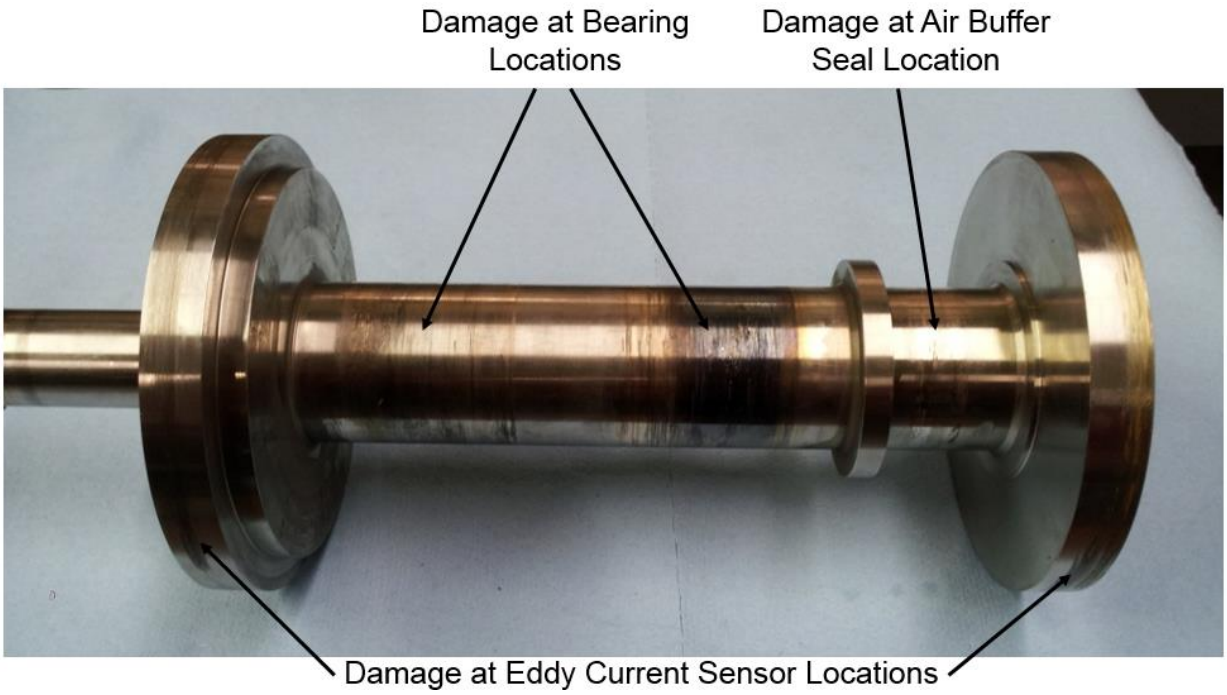


**Figure 22. Photograph of rotor after failure (2013) [10].**

Figure 23 shows the rotor after being repaired and balanced. In the locations where the air buffer seals and the eddy current sensors deposited foreign material, WD-40 and 600-grit sandpaper polished off the foreign material. In the locations of the journal bearings, Multichrome/Microplate Company grinded off the affected material, chrome-plated the rotor with 76.2 micron of thin-dense chrome, and grinded the rotor until the rotor diameter was its original size for a cost of $958. This process replaced the affected material with thin-dense chrome. Moscow Mills balanced the new rotor by grinding off significantly more material than the original rotor had ground off at a cost of $787.

**Figure 23. Photograph of rotor after being polished, pre-grinded, chrome-plated, post-grinded, and balanced (March 2014).**

Table 4 shows the measured diameter of the rotor at the journal bearing locations and the thrust collars. The average diameter at the locations that interface with the journal bearings are 38.100 mm and 38.102 mm. These are within the tolerance of ±5 μm. The average rotor diameter at the thrust collars is 101.68 mm and 106.69 mm. The maximum deviation in the diameter at the journal bearing locations is 10.2 μm. The maximum deviation in the diameter on the thrust collars is 12.7 μm.

**Table 4. Diameter of rotor at journal bearing locations and thrust collars.**

| Axial Location | Average [mm] | Standard Deviation [μm] | Uncertainty [μm] | Maximum Deviation [μm] |
|---|---|---|---|---|
| Slave Bearing Collar | 106.69 | 3.58 | ± 7.6 | 10.2 |
| Motor Side Journal Bearing | 38.100 | 2.46 | ± 5.2 | 10.2 |
| Free Side Journal Bearing | 38.102 | 2.05 | ± 4.3 | 7.6 |
| Test Bearing Collar | 101.61 | 3.78 | ± 8.0 | 12.7 |

### Mass Properties

Table 5 shows the rotor measured and predicted mass, center of mass, and mass moments of inertia. XLTRC$^2$, a rotordynamic software, predicts the mass properties. The appendix describes the apparatus and procedure for predicting and estimating the rotor mass properties. The mass of the rotor is 3.856 kg with its center of mass 15.38 cm away from the coupling end. The transverse and polar mass moments of inertia are 263.2 kg-cm$^2$ and 31.1 kg-cm$^2$, respectively. The predicted rotor mass properties compare well to the measurements.

**Table 5. Rotor mass, center of mass, and mass moments of inertia: measurements and predictions.**

| Mass Property | Measurement | Prediction | Percent Difference |
|---|---|---|---|
| Mass [kg] | 3.856 ± 0.014 | 3.874 | 0.47 |
| Center of Mass [cm] | 15.38 ± 0.10 | 15.49 | 0.42 |
| Transverse Mass Moment of Inertia [kg-cm$^2$] | 263.2 ± 19.5 | 253.2 | 3.79 |
| Polar Mass Moment of Inertia [kg-cm$^2$] | 31.1 ± 2.63 | 30.80 | 0.92 |

## Free-Free Mode Natural Frequency

Table 6 and Figure 24 show the rotor free-free mode natural frequency, measured and predicted, and the corresponding mode shapes. XLTRC$^2$ predicts the rotor free-free natural frequency and mode shape. Appendix D describes the apparatus and procedure for measuring the free-free natural frequencies and mode shapes. The measured first free-free natural frequency is 1760 Hz. The rotor end facing the coupling experiences the highest amplitude displacements. The predicted natural frequency is 1830 Hz, 4% higher than the measured natural frequency. The measured and predicted mode shapes of the rotor first mode compare well to each other.

**Table 6. Measured and predicted first free-free natural frequency of rotor.**

| | Measured Frequency [Hz] | Predicted Frequency [Hz] | Percent Difference |
|---|---|---|---|
| 1$^{st}$ Free-Free Natural Frequency | 1760 ± 8 | 1830 | 4.0 |

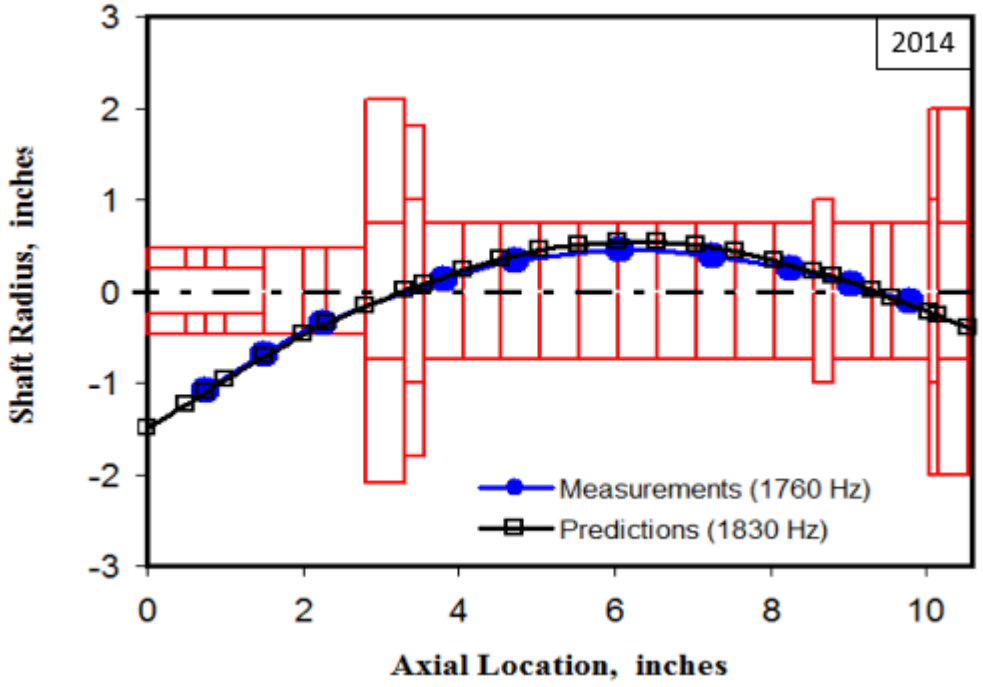


**Figure 24. Measured and predicted first free-free mode shape of rotor.**

## Flexible Coupling

The flexible coupling, as shown in Figure 25, broke during the emergency stop initiated during the failure. The unscheduled, sudden stop placed a large torque on the coupling, producing a torsion that ruptured the (flexible) diaphragm.

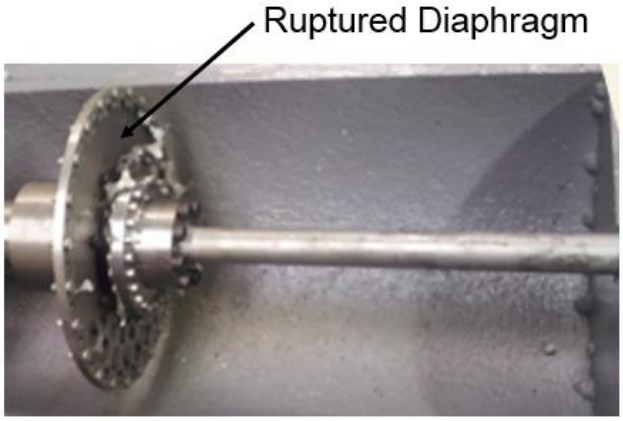


**Figure 25. Photograph of flexible coupling after failure (2013) [10].**

Figure 26 shows the repaired coupling, early 2014. At a cost of $6,780, the original manufacturer replaced the diaphragm and the outer hub ring and reused other original parts, and then balanced the new assembly.

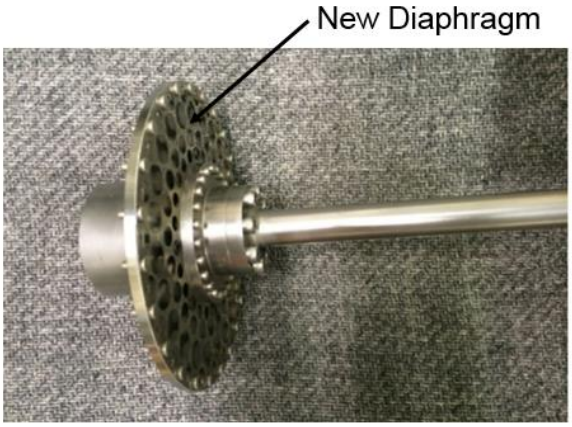


**Figure 26. Photograph of flexible coupling after repair by Coupling Corporation of America.**

## Mass Properties

Table 7 shows the flexible coupling measured and predicted mass properties. XLTRC$^2$ predicts the mass properties. The mass of the coupling is 1.15 kg; its center of mass is 9.05 cm away from the clamp end. The transverse and polar mass moments of inertia are 128.7 kg-cm$^2$ and 8.16 kg-cm$^2$, respectively. The predictions and the measurements for the transverse mass moment of inertia show slight differences because of the complex geometry of the coupling.

**Table 7. Flexible coupling mass, center of mass, and mass moments of inertia: measurements and predictions.**

| Mass Property | Measurement | Prediction | Percent Difference |
|---|---|---|---|
| Mass [kg] | 1.150 ± 0.010 | 1.21 | 5.30 |
| Center of Mass [cm] | 9.05 ± 0.10 | 8.66 | 1.15 |
| Transverse Mass Moment of Inertia [kg-cm$^2$] | 128.7 ± 8.53 | 109.9 | 14.58 |
| Polar Mass Moment of Inertia [kg-cm$^2$] | 8.16 ± 0.66 | 7.90 | 3.17 |

## Free-Free Mode Natural Frequencies

Table 8 and Figure 27 and 28 show the measured and predicted first and second natural frequencies of the flexible coupling and corresponding free-free mode shapes. XLTRC$^2$ predicts the free-free natural frequencies and mode shapes. The first and second free-free natural frequencies of the coupling are 496 Hz and 1504 Hz, respectively. The first natural frequency is particularly important because the maximum operating speed of the motor is 500 Hz and it is close to the rotor speed when the failure occured. The coupling vibrates with the highest amplitude at the end that attaches to the rotor. The predictions for the free-free natural frequencies and mode shapes compare well to the measurements.

**Table 8. Measured and predicted first and second free-free mode natural frequencies of flexible coupling.**

| | Measured Frequency [Hz] | Predicted Frequency [Hz] | Percent Difference |
|---|---|---|---|
| 1st Free-Free Natural Frequency | 496 ± 8 | 487 | 1.8 |
| 2nd Free-Free Natural Frequency | 1504 ± 8 | 1524 | 1.3 |

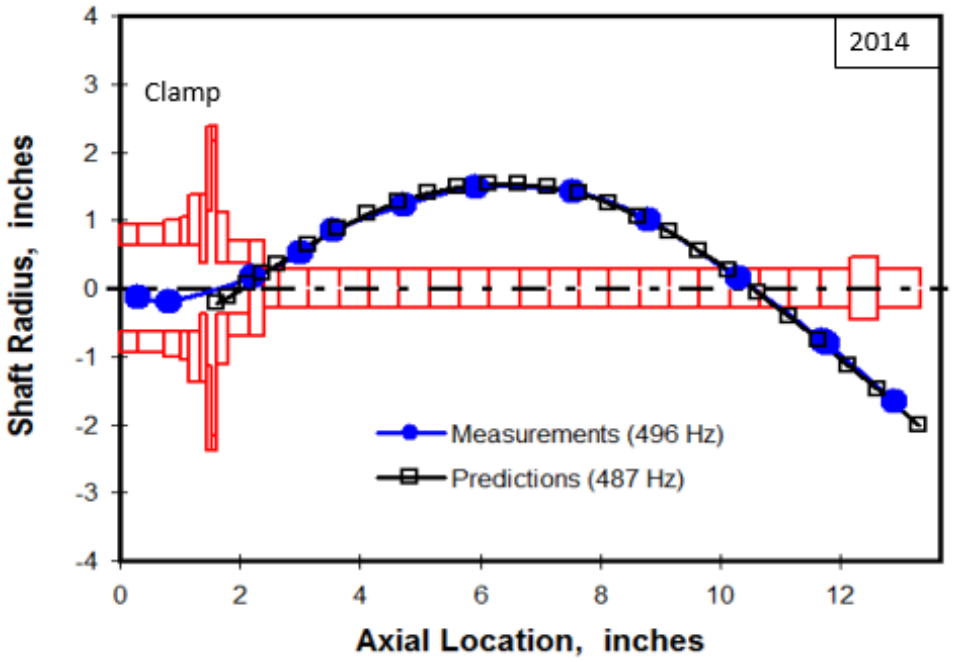


**Figure 27. Measured and predicted first free-free mode shape of coupling.**

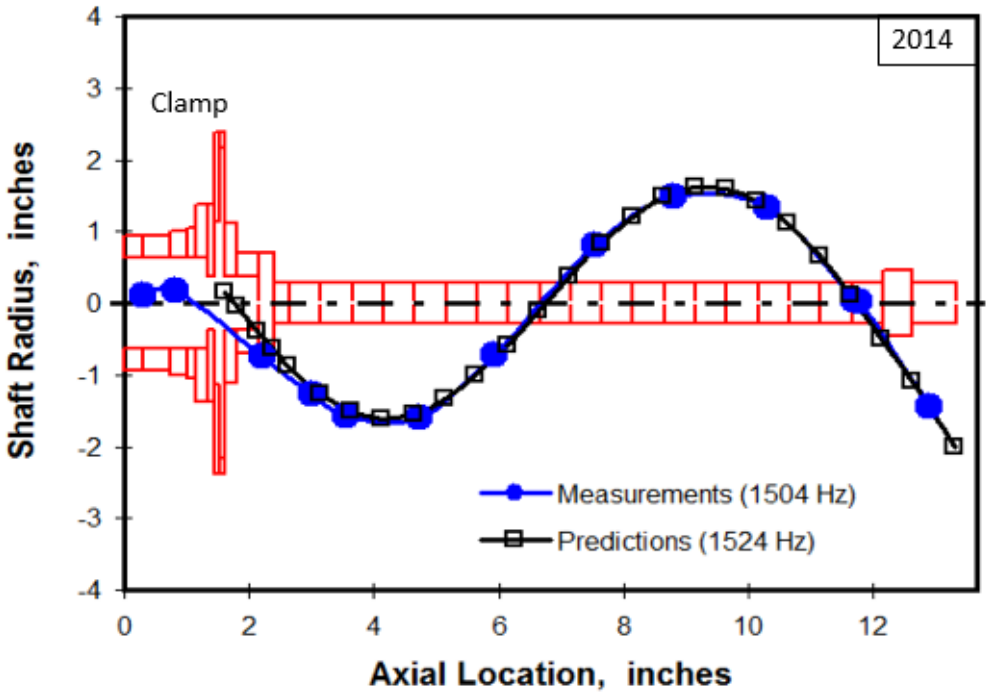


**Figure 28. Measured and predicted second free-free mode shape of coupling.**

# Revamping the Test Rig

## Journal Bearings and Slave Thrust Bearing

Figure 29 shows the damaged (air lubricated) flexure pivot tilting pad hydrostatic journal bearings. The contact between the rotor and the journal bearings during failure produced significant heat that welded the flexural pads to the bearing making them useless. Figure 30 shows the original water lubricated flexure pivot, tilting pad bearings that replace the damaged bearings.

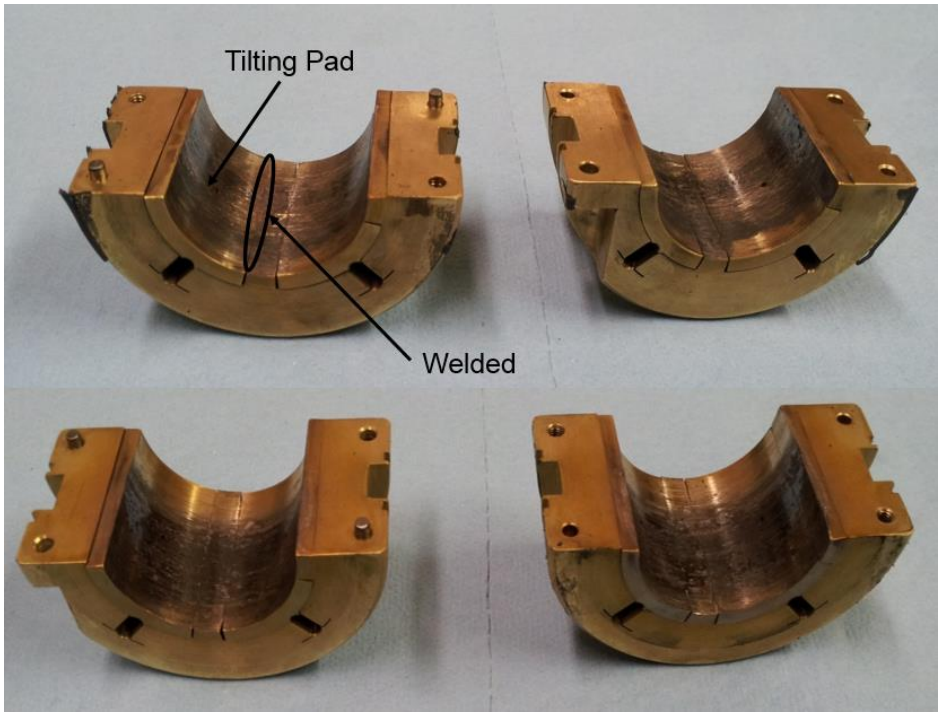


**Figure 29. Photograph of air lubricated journal bearings after failure (2013) [10].**

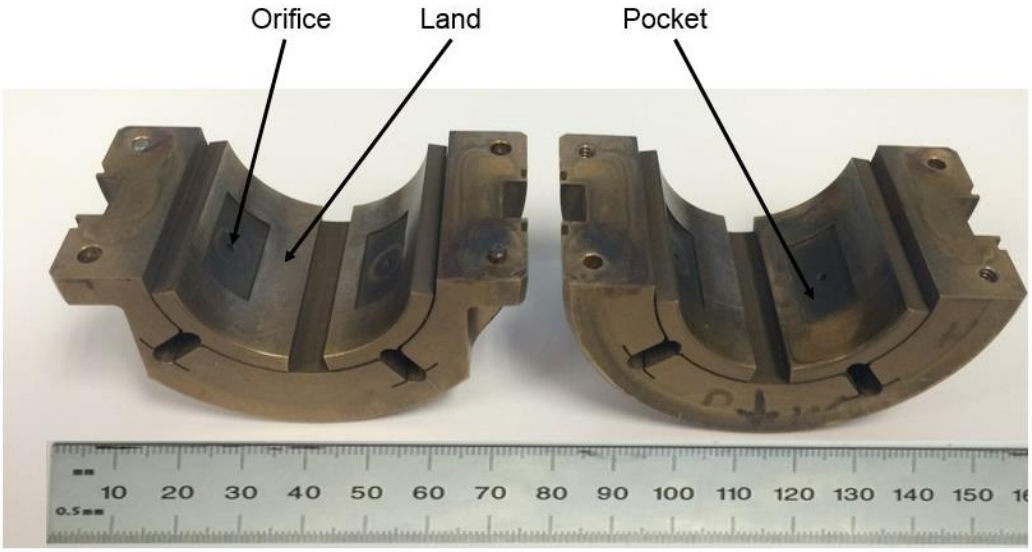


**Figure 30. Photograph of original flexure pivot, tilting pad journal bearings with water lubrication.**

Figure 31 shows the slave thrust bearing[1] that the rotor contacted during the test rig failure. The rotor roughened the face of the slave bearing. Figure 32 shows the repaired slave bearing. The removal of the epoxy from the pockets enables the slave bearing to run with water lubrication,

1. The pockets were covered with epoxy to increase the land surface area and enable the bearing to operate with air.

which is the same fluid that lubricates the journal bearings. The TAMU aerospace machine shop lapped off 63.5 μm the face of the slave bearing, providing a smooth surface. The pockets of the repaired slave bearing are presently 444 μm deep.

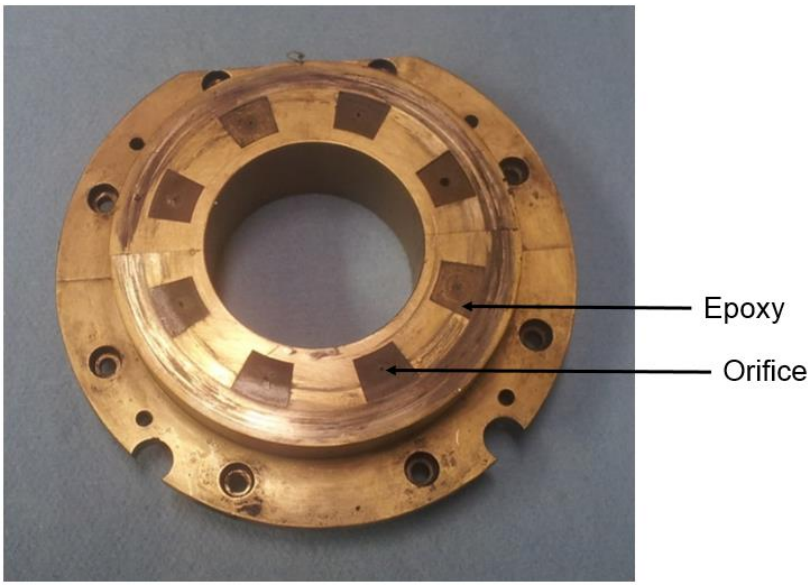


**Figure 31. Photograph of damaged slave thrust bearing [10].**

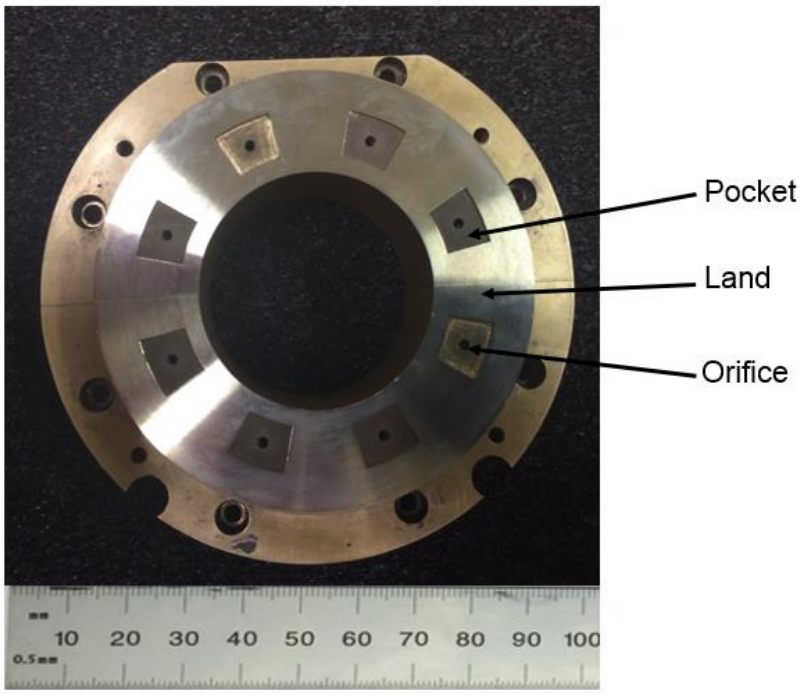


**Figure 32. Photograph of current condition of slave thrust bearing with epoxy removed and lapped surface.**

Presently the journal bearings and slave bearing operate with water as the lubricating fluid. Figure 33 shows the water manifold that (5.86 bar) water flows through before entering the test rig. The manifold and its instrumentation provide the means to regulate the flow and inlet pressure, and measure the inlet temperature, pressure, and flow rate of the water delivered to the test bearing. The manifold also includes valves to shut off the flow and a relief route to flow the water around the test rig. Figure 34 shows the exhaust hoses for the water to flow out of the test rig. The PVC pipe on the floor transfers the water to outside the test cell.

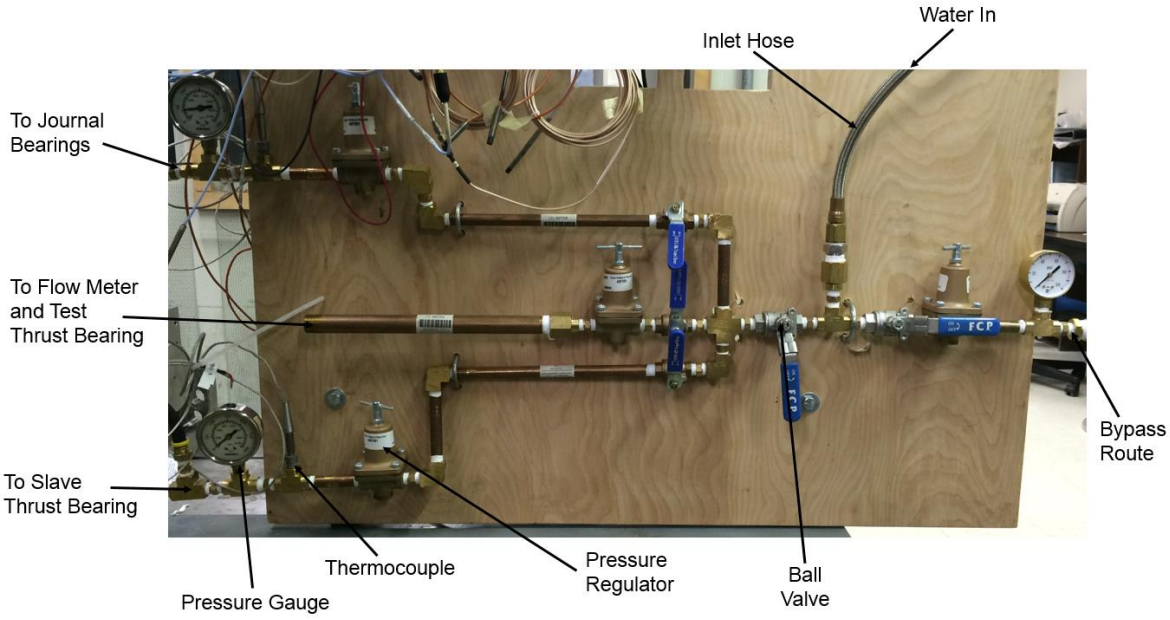


**Figure 33. Photograph of water manifold.**

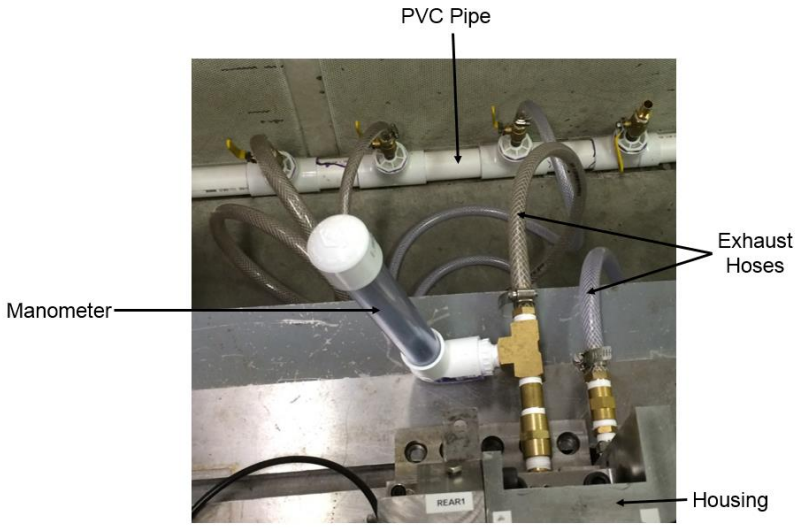


**Figure 34. Photograph of exhaust piping.**

## Air Buffer Seals

Figure 35 shows the motor side and free side air buffer seals after the failure. When the rotor experienced large amplitude motions, the rotor contacted the air buffer seals. The contact between the rotor and the air buffer seals caused them to deform at the inner diameter of the interface between the top and bottom halves of each seal. Once the rotor motions became large enough, the pins and screws that attached the seals to the housing sheared off. The protruding deformations were removed, enabling the air buffer seals to close completely. Hardened steel pins align the seals with the housing. Epoxy cold-welds the air buffer seals onto the housing, shown in Figure 36.

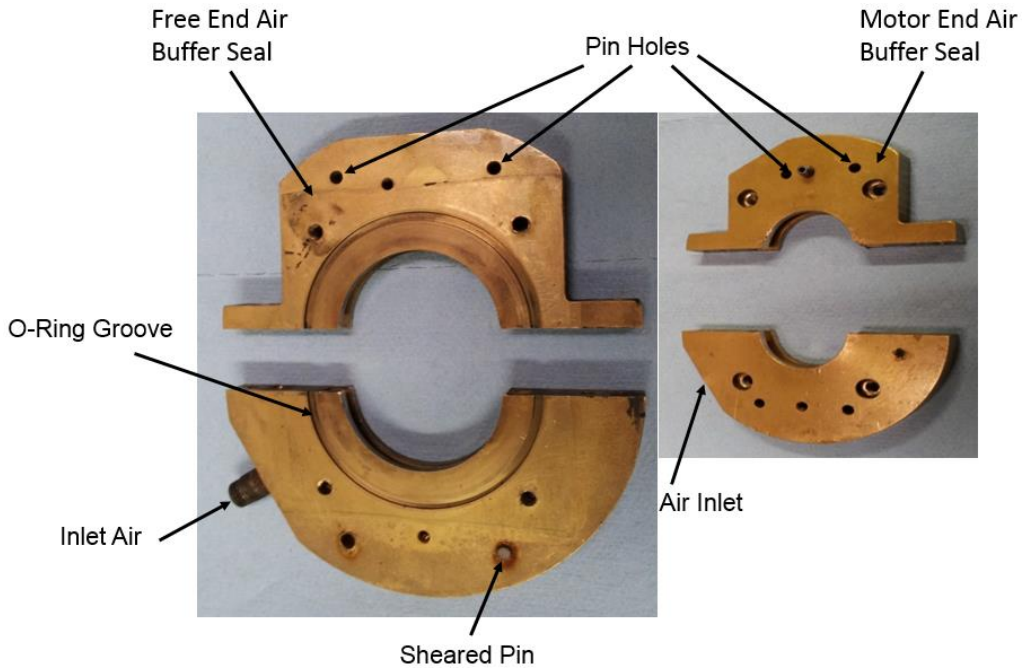


**Figure 35. Photograph of motor side and free side air buffer seal after failure [10].**

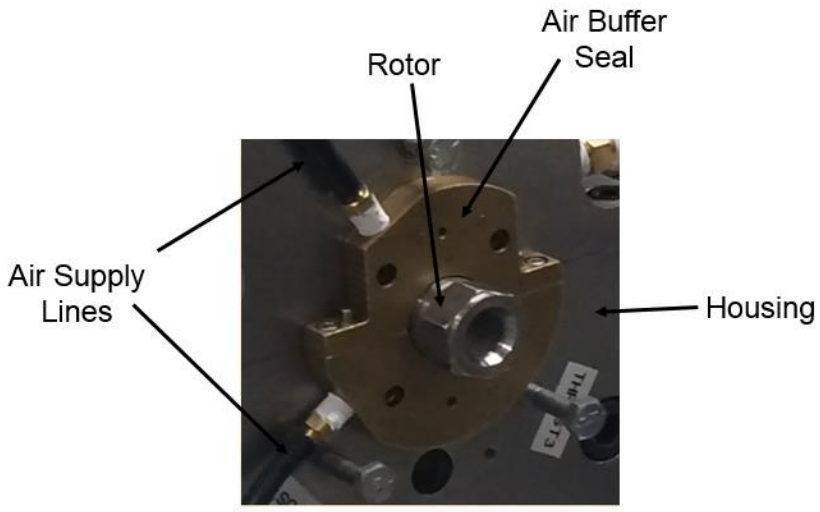


**Figure 36. Photograph of air buffer seal on the housing.**

## Housing

The housing did not suffer any damage in the failure, but it undergoes disassembly and reassembly in order to fix the parts within it. RTV (room temperature vulcanizing) silicone gasket lines the journal bearing housing, and cap screws close the journal bearing housing forcing the RTV to make a seal. Bolts connect the slave bearing housing to the journal bearing housing, as shown by Figure 37. RTV applies a seal at the interface between the different components of the housing.

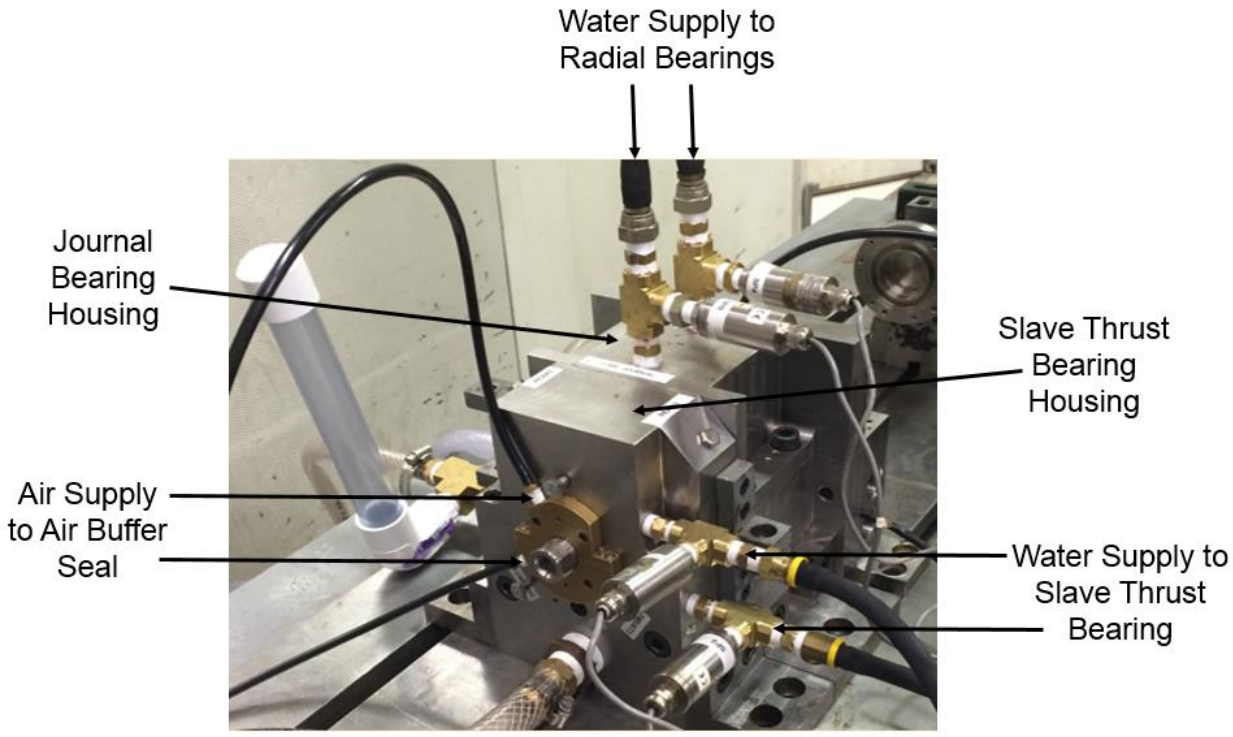


**Figure 37. Photograph of journal and slave bearing housings assembled with water and air lines connected.**

## Closure

The thrust bearing test rig is being revamped to provide reliable experimental results to validate predictions in order to improve the design of thrust bearings. Previously, the test rig showed remarkable correlations between predictions and experimental results of water lubricated hybrid thrust bearings [2].

The test rig was modified to operate with air lubrication. During its maiden operation, the rotor experience large amplitude vibrations, and then the operator initiated an emergency stop. The large amplitude vibrations caused the rotor to rub against the journal bearings, the slave thrust bearing, and the air buffer seals. The contact caused foreign material to weld onto the surface of the rotor, the tilting pads of the air lubricated journal bearings to weld to the bearing cartridge, the surface of the slave thrust bearing to be damaged, and the air buffer seal screws to shear off the housing. The large torsion produced from the emergency stop caused the flexible coupling diaphragm to rupture [3].

An electroplating company repaired the rotor by grinding off the affected areas, chrome-plating thin-dense chrome back on, and grinding back down to the correct diameter. A balancing company then balanced the rotor. The original manufacturer of the coupling repaired it by replacing the

flexible diaphragm and rebalancing it. The original, water journal bearings replace the air journal bearings. A campus machine shop lapped the surface of the slave thrust bearing to provide a smooth surface. The test rig was assembled with the repaired and replaced components. The test rig is capable of testing thrust bearings at rotor speeds up to 20 krpm and loads up to 600 newtons.

The main objective of the work for the next year is to measure the performance of a hybrid thrust bearing (eight pocket) lubricated with water. The test rig could also be used to test other bearings with a 3-inch outer diameter at speeds up to 20 krpm. The first task will be to complete the revamping of the test rig, which includes aligning the rotor, and installing the instrumentation. The second task will be to measure the minimum film thickness versus thrust load for a water lubricated hybrid thrust bearing at rotor speeds up to 20 krpm and supply pressures up to 6 bar.

## References


[1] San Andrés, L., 2013, "A Test Rig for Evaluation of Thrust Bearings and Face Seals," TAMU Proposal to TRC, *Turbomachinery Laboratory, Texas A&M University*

[2] Esser, P., 2010, "Measurements versus Predictions for a Hybrid (Hydrostatic plus Hydrodynamic) Thrust Bearing for a Range of Orifice Diameters," Master's Thesis, *Turbomachinery Laboratory, Texas A&M University*

[3] Park, S., 2013 "Failure Report for Air Bearing Test Rig," Internal Report, *Turbomachinery Laboratory, Texas A&M University*

[4] Gregory, R.S., 1974, "Performance of Thrust Bearings at High Operating Speeds," *ASME J. Tribol.*, **96** (1) pp 7-14

[5] Glavatskih, S.B., 2002, "Laboratory Research Facility for Testing Hydrodynamic Thrust Bearings," *ASME J. Tribol.*, **216** (2), pp 105-116

[6] Dykas, B.D. and Tellier, D.W., 2008, "A Foil Thrust Bearing Test Rig for Evaluation of High Temperature Performance and Durability," *Army Research Laboratory*, pp 1-14

[7] Dadouche, A., Fillon, M., and Dmochowski, W., 2006, "Performance of a Hydrodynamic Fixed Geometry Thrust Bearing: Comparison between Eperimental Data and Numerical Results," *Tribology Transactions*, **49** (3), pp 419-426

[8] Balducchi, F., Arghir, M., Gauthier, R., and Renard, E., 2013, "Experimental Analysis of the Start-Up Torque of a Mildly Loaded Foil Thrust Bearing," *ASME J. Tribol.*, **135**, pp 1-7

[9] San Andrés, L., 2011, "Description of a Thrust Bearing Test Rig," *Turbomachinery Laboratory, Texas A&M University*

[10] Park, S., July 2013, "Failed Parts," Internal Progress Report, *Turbomachinery Laboratory, Texas A&M University*

[11] San Andrés, L., Rohmer, M., 2014, "Measurements and XLTRC$^2$ Predictions of Mass Moments of Inertia, Free-Free Natural Frequencies and Mode Shapes of Rotor and Flexible Coupling," Internal Progress Report, *Turbomachinery Laboratory, Texas A&M University*

[12] Andriulli, J. B., 1997, "A Simple Way to Measure Mass Moments of Inertia," *Sound and Vibration*, pp. 18-19.

# Appendices

## Appendix A

**Table 9. Costs of repairs.**

| Purchase | Vendor | Cost |
|---|---|---|
| Grinding and chromeplating rotor | MultiChrome/Microplate Company | $957.50 |
| Balancing rotor | Moscow Mills, Inc. Vibration Soultions North | $787.00 |
| Repairing coupling | Coupling Corporation of America | $6780.00 |
| Building water manifold | Grainger and Bryan Hose & Gasket | $943.66 |
| Adjacent piping | Grainger | $501.06 |
| Hardware and tools | Grainger | $253.15 |
| Total | | $10,271.37 |

# Appendix B

**Table 10. Instrumentation for thrust bearing test rig.**

| Instrumentation | Measurement | Quantity |
|---|---|---|
| Eddy current sensors | Rotor lateral motions at each thrust collar, 2 x 2 (X,Y) | 4 |
| Eddy current sensors | Rotor axial and tilt motions at each thrust collar, 2 x 3 (120°) | 6 |
| Strain gauge pressure sensor | Pressure in pockets (2) and on land (1) of test thrust bearing | 3 |
| Pressure transducers | Supply pressure of each bearing and air buffer seals, discharge pressure of test thrust bearing | 8 |
| Pressure regulators | Control supply pressure of each bearing | 4 |
| Thermocouples | Inlet temperature of each bearing and discharge temperature of test thrust bearing | 4 |
| Turbine flow meters | Flow into test thrust bearing and flow out of inner diameter of test thrust bearing | 2 |
| Tachometer | Rotor speed | 1 |
| Load cell | Axial load applied by shaker | 1 |

# Appendix C

## Set Up and Procedure to Identify Mass Properties [11]

Figure 38 portrays the rotor suspended horizontally from two inextensible strings. to estimate its transverse mass moment of inertia ($I_T$). In the figure, $r$ is the distance between a string and the center of mass, and $L \approx 1$ m is the length of the inextensible string.

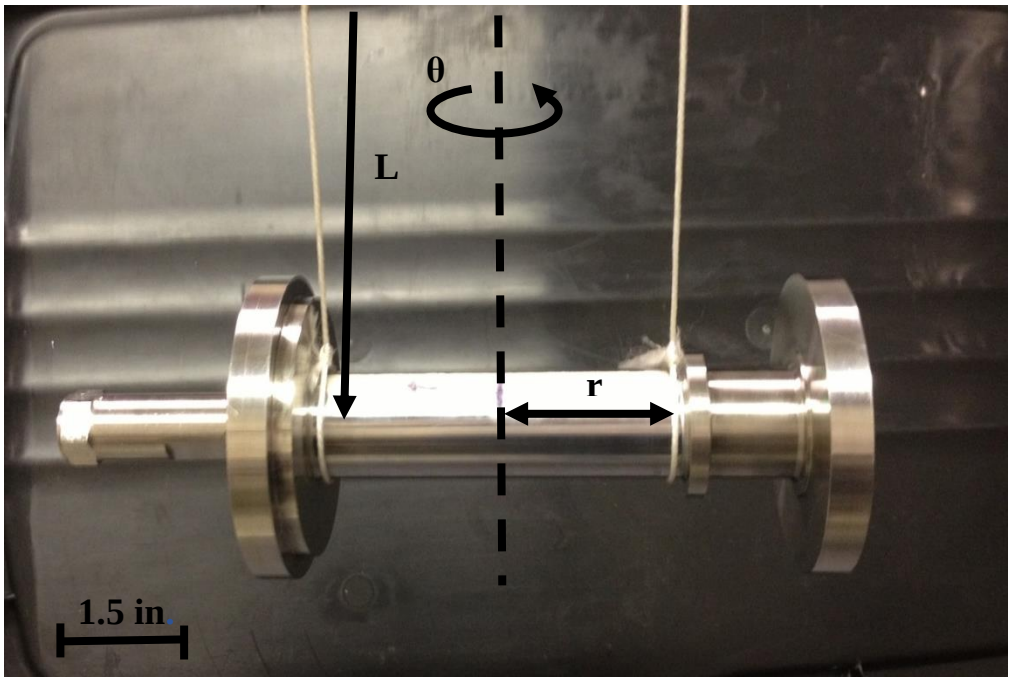


**Figure 38. Photograph of rotor suspended horizontally to estimate its transverse mass moment of inertia.**

The rotor is displaced to a small angular displacement and released. Once released, the rotor oscillates like a pendulum around its equilibrium point. A stopwatch measures the time elapsed between ten cycles. Andriulli [12] shows that the transverse mass moment of inertia of the rotor is determined from:

$$I = \frac{mg}{L}\left(\frac{r}{2\pi f}\right)^2$$

where $f$ is the natural frequency of oscillation [Hz]. The same set up and process delivers the polar mass moment of inertia of the rotor and both the transverse and polar mass moments of inertia of the coupling.

Figure 39 shows the model of the rotor built in XLTRC$^2$. The model divides the rotor into 25 stations of stainless steel 316 or Inconel 718.

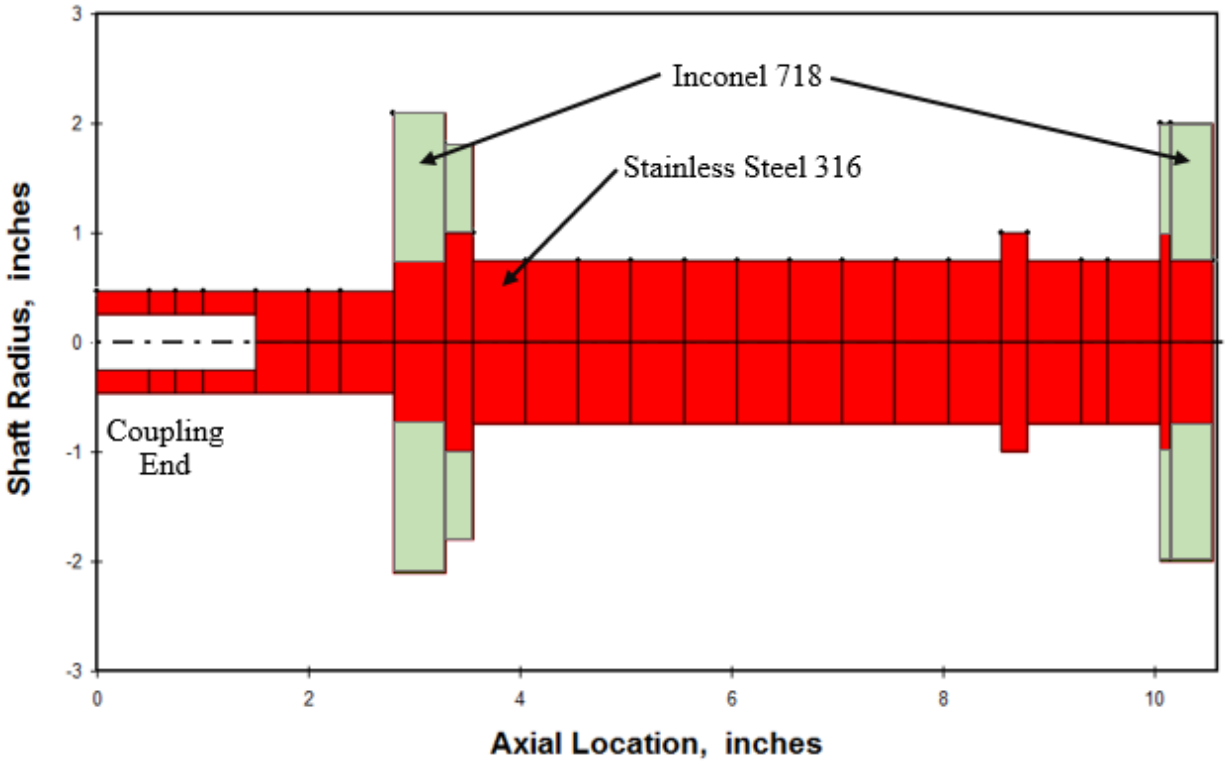


**Figure 39. XLTRC$^2$ Model of rotor.**

Figure 40 shows the coupling modeled in XLTRC$^2$ as a rigid shaft. This model does not consider the flexibility introduced by the diaphragm. This model predicts mass properties only. The model divides the coupling into 34 stations of alloy steel 4140.

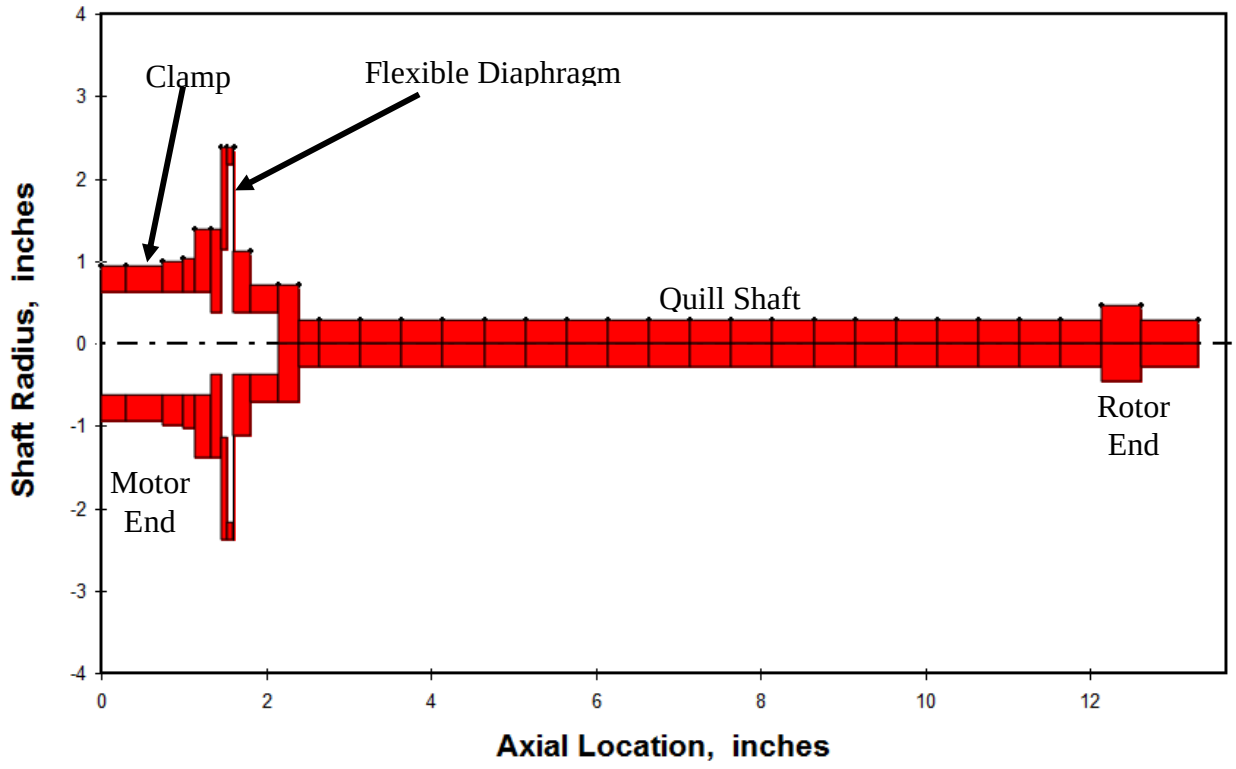


**Figure 40. Model of entire coupling as a rigid shaft in XLTRC[2].**

## Appendix D

### Set Up for Measuring Natural Frequencies and Mode Shapes [11]

Figure 41 shows the rotor suspended from two 8 ft. long strings. The strings provide negligible stiffness in the direction orthogonal to their length. Wax holds two 1 gram piezoelectric accelerometers to the rotor. One reference accelerometer remains stationary at the center of mass of the rotor.[2] The other accelerometer roams to various stations on the rotor. It is important that the accelerometers are mounted orthogonal to the length of the string. Cables connect the accelerometers to a dynamic signal analyzer.

2. It is not necessary that the reference accelerometer is at the center of mass, but it should not be located at a vibration node.

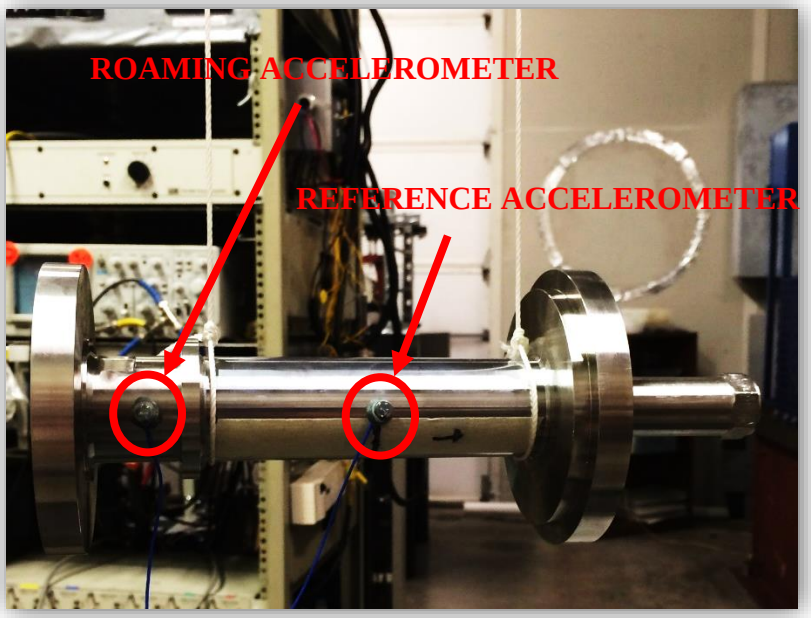


**Figure 41. Photograph of rotor suspended with accelerometers mounted on it.**

The same set up serves to measure the natural frequencies and mode shapes of the flexible coupling.

## Procedure

A hammer with a plastic tip strikes the rotor and excites it, as shown with a schematic in Figure 42. The hardness of the tip must not cause damage to the rotor or the coupling. The dynamic signal analyzer measures and records the amplitude of acceleration, the natural frequency, and the phase angle between the two accelerometers. The dynamic signal analyzer measures five averages of ten impulses. Wax affixes the roaming accelerometer to nine other locations, and the process listed above is repeated. The relative amplitudes and phase angles between the two accelerometers at different locations determine the mode shape at each frequency. The same procedure serves to measure the natural frequencies and mode shapes of the flexible coupling.

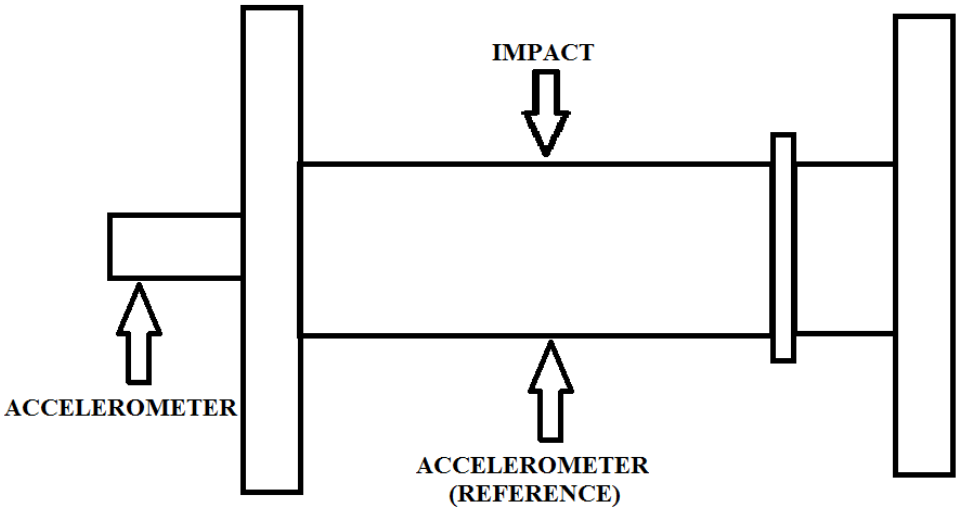


**Figure 42. Schematic view of rotor with locations of impact and accelerometers.**

Figure 43 shows the model of the rotor in XLTRC$^2$. The model divides the rotor into 25 stations of stainless steel 316 or Inconel 718.

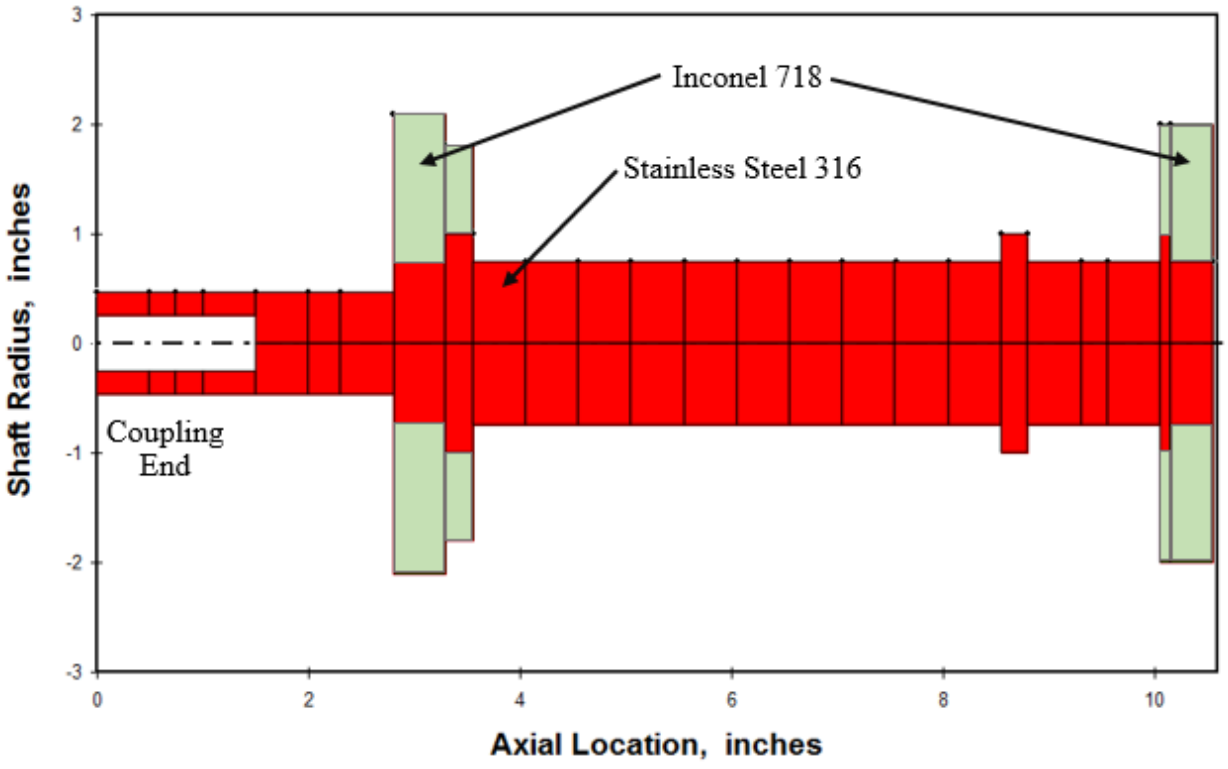


**Figure 43. Model of rotor in XLTRC$^2$.**

Figure 44 shows the model for the quill shaft of the coupling with the clamp as a point mass at the diaphragm location. This model predicts the natural frequencies and mode shapes of the

coupling. This model assumes that the flexible diaphragm isolates the quill shaft from the inertia of the other side of the diaphragm but not the mass.

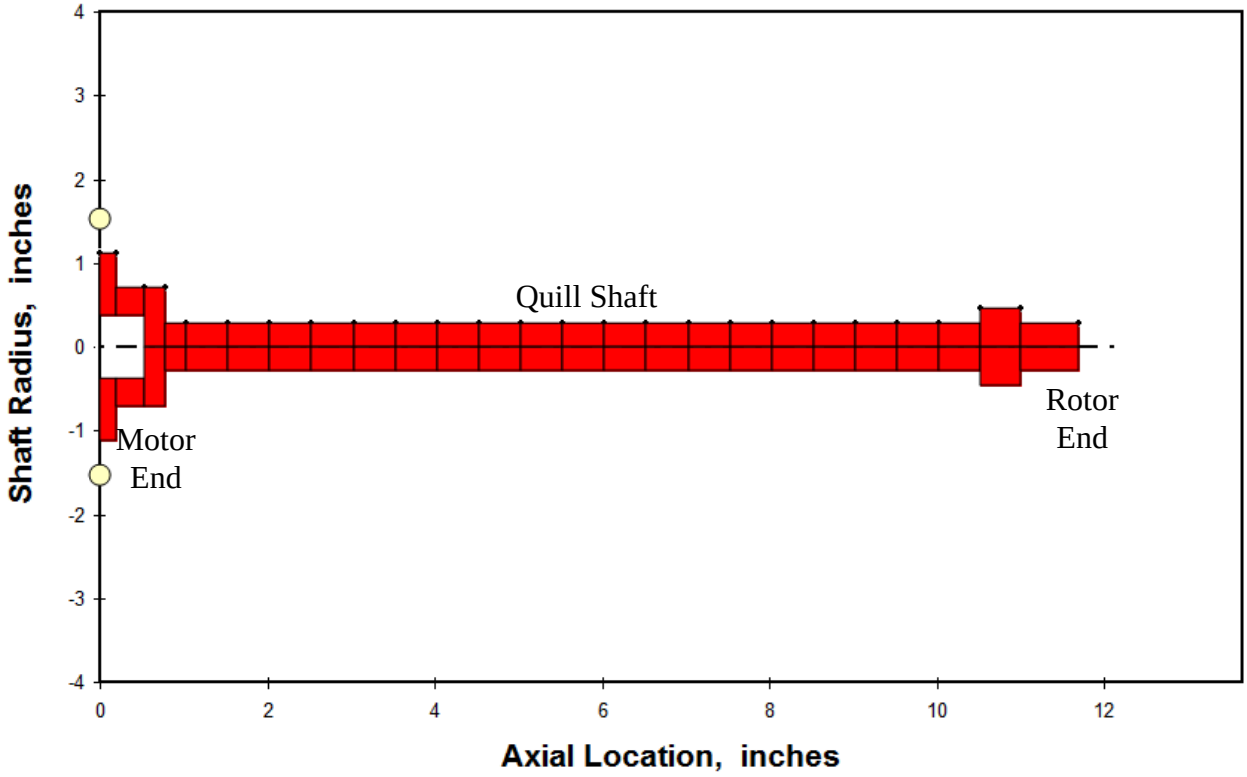


**Figure 44. XLTRC$^2$ model of quill shaft of coupling with clamp as a point mass.**